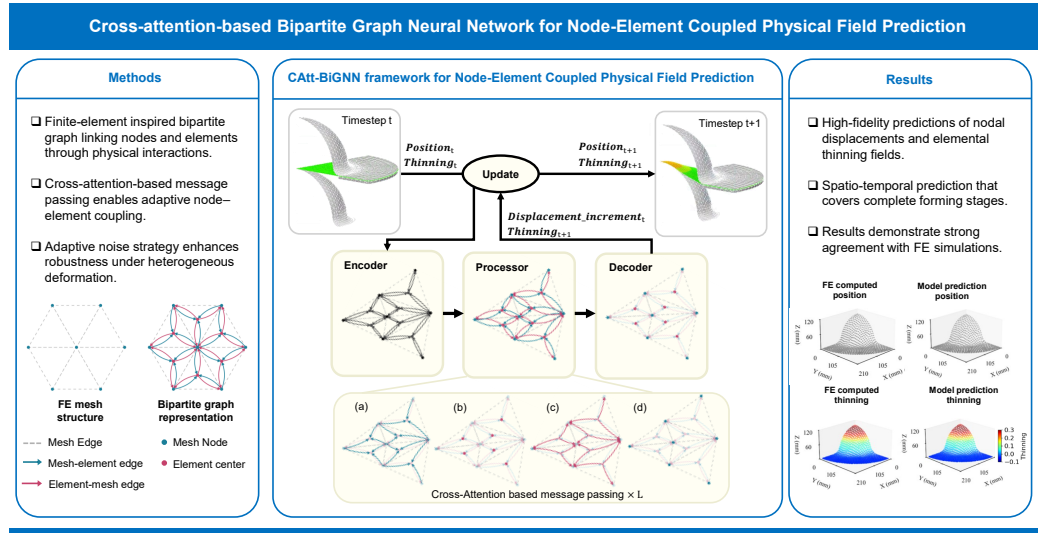


Graphical Abstract

Cross-attention-based bipartite graph neural network for coupled nodal and elemental field prediction in large-deformation sheet material forming

Yingxue Zhao, Haoran Li, Haosu Zhou, Tobias Pfaff, Nan Li



Y. Zhao, H. Li, H. Zhou, T. Pfaff, N. Li (2026)
 Corresponding author: Nan Li (n.li09@imperial.ac.uk)

Highlights

Cross-attention-based bipartite graph neural network for coupled nodal and elemental field prediction in large-deformation sheet material forming

Yingxue Zhao, Haoran Li, Haosu Zhou, Tobias Pfaff, Nan Li

- A cross-attention-based bipartite graph neural network is proposed for sheet forming.
- Bipartite graphs enable joint prediction of nodal and elemental states.
- Edge-aware cross-attention learns adaptive node–element coupling.
- A hierarchical extension improves propagation on larger graphs.
- Adaptive Gaussian noise improves robustness in autoregressive rollout predictions.

Cross-attention-based bipartite graph neural network for coupled nodal and elemental field prediction in large-deformation sheet material forming

Yingxue Zhao^a, Haoran Li^a, Haosu Zhou^a, Tobias Pfaff^b, Nan Li^{a,*}

^a*Dyson School of Design Engineering, Imperial College London, London, UK*

^b*NVIDIA, UK*

Abstract

Finite element simulations of large-deformation sheet material forming involve node-element coupling between nodal kinematics and element-level deformation measures. Machine-learning surrogates can accelerate such simulations, but most graph-based models use node-centred representations. This representation is indirect for element-level quantities, which are often recovered from nodal predictions by interpolation or post-processing. It may also obscure the node-element coupling structure that underlies the finite element update. This work proposes a cross-attention-based bipartite graph neural network (CAtt-BiGNN) for coupled prediction of nodal displacement increments and elemental thinning. The graph represents mesh nodes and elements as distinct but connected entities, linked by directed node-element edges, so that nodal and elemental fields are predicted on their native discretisation domains. An edge-aware cross-attention processor conditions adaptive node-element coupling weights on geometric edge features, enabling bidirectional message passing between nodal kinematic states and elemental deformation states. A hierarchical extension, CAtt-BiUGNN, combines the CAtt-BiGNN with graph downsampling-upsampling to improve information propagation on larger meshes. Adaptive Gaussian noise is further evaluated as an optional rollout-stabilisation strategy. The models are tested on two representative forming cases with different graph sizes. CAtt-BiGNN improves the balance between displacement and thinning prediction relative to node-centred baselines and bipartite ablation variants, while CAtt-BiUGNN gives

*Corresponding author. E-mail address: n.li09@imperial.ac.uk (N. Li)

the strongest overall performance in the larger-graph setting. The results indicate that the proposed model provides an effective surrogate framework for large-deformation sheet material forming.

Keywords: Sheet material forming, Surrogate modelling, Graph neural networks, Bipartite graph, Deformation prediction, Cross-attention mechanism, Hierarchical graph neural network

1. Introduction

Finite element analysis (FEA) is the primary computational tool for predicting deformation behaviour in solid mechanics. It provides access to both nodal kinematics and elemental deformation measures, such as strains, stresses, and thickness changes [1, 2, 3]. Nodal displacements drive the deformation of elements. Elemental quantities evaluated at integration points contribute back to the nodal equilibrium through the assembly of internal forces in the finite element formulation. Accurately capturing this bidirectional coupling is essential for predicting deformation behaviour, strain localisation, and other failure-related phenomena across many engineering applications. However, the computational cost of high-resolution finite element simulations can become restrictive when large design spaces are explored or when iterative optimisation is required [4, 5]. In recent years, machine learning (ML)-based surrogate modelling has emerged as an effective approach to accelerate finite element analysis while maintaining the accuracy required for engineering applications [6, 7].

Building on this idea, machine learning-based surrogate models have increasingly been explored in computational solid mechanics to approximate the response of complex physical systems [8, 9, 10]. Among the available approaches, graph neural networks (GNNs) have emerged as particularly well suited for mesh-based simulations because they naturally operate on irregular graph structures that resemble finite element meshes [11, 12, 13, 14]. This representation enables the modelling of connectivity relationships between mesh entities such as nodes and edges [15, 16, 17], allowing physical fields such as displacements, stresses, and strains to be directly learned from mesh-based data [18, 19]. As a result, GNN-based surrogate models have demonstrated promising performance across a range of mechanics-related simulation tasks [7, 20, 21, 22].

However, most existing mesh-based GNN surrogates adopt a node-centred

formulation in which the primary predicted quantities are associated with mesh nodes [12, 23, 24, 25, 26]. This design is effective when the target fields are nodal variables, such as displacement or acceleration. It is less direct when the quantities of interest are element-level or integration-point variables, such as strain, stress, or thinning. In such cases, elemental fields are often recovered from nodal predictions through interpolation, projection, or post-processing. This additional mapping can introduce errors and may obscure the native finite-element relation between nodal kinematics and element-level deformation measures. The issue is particularly important in sheet material forming, where thinning is naturally evaluated at the element or integration-point level and is a key indicator of localisation and forming quality.

This limitation points to the need for a representation that more closely reflects the information flow in the finite element update cycle. Instead of representing nodal and elemental quantities into a single node-centred graph state, a surrogate model may benefit from representing different FE mesh entities on their native discretisation domains and learning their interactions through data-driven message passing. In this view, the graph structure acts as a finite-element-inspired inductive bias: mesh nodes and elements are treated as distinct but coupled entities, and their information exchange is organised to resemble the transfer between nodal kinematics and element-level deformation measures in the FE formulation. Such a representation does not impose the finite element equations explicitly, but it provides a structured pathway through which the model can exploit node–element coupling patterns present in the simulation data.

Related efforts have also recognised that the choice of graph representation is important for mesh-based surrogate modelling. Several studies have moved beyond conventional node-based graphs by embedding elemental or boundary-related information more directly into the graph structure [27, 28, 29]. The Boundary Oriented Graph Embedding (BOGE) method maps geometric and boundary information onto elemental vertices [27], while Zhou et al. [28] developed multi-level element-based GNN models for predicting elemental thinning fields. These studies show that graph representations can be adapted to better reflect the quantities of interest in finite element simulations. However, these studies primarily focus on the representation or prediction of elemental information, with less emphasis on the coupled interaction between nodal and elemental states in the surrogate formulation.

Recent work has further explored graph structures that encode numerical-

discretisation relations more explicitly [30, 31]. In such formulations, an element or control volume can be represented as a hyperedge connecting its associated mesh nodes, thereby embedding element–node relations directly within the graph. For example, finite-volume-inspired GNNs use control-volume-based hyperedges to support flux exchange between neighbouring volumes [30], and finite-element-inspired hypergraph models incorporate element–node connectivity and update rules derived from discretised governing equations [31]. These approaches strengthen the link between graph learning and numerical discretisation. Nevertheless, the present large-deformation sheet forming problem involves the coupled evolution of nodal kinematics and element-level deformation variables, including thinning, within a dynamic rollout setting. This motivates a bipartite representation in which nodal and elemental states are both retained and coupled through learnable node–element interactions.

For large-deformation sheet material forming, this node–element coupling is directly tied to the displacement-based finite element update. Elemental deformation measures, such as strain, stress, and thinning evaluated at integration points, are computed from nodal kinematics, while the resulting elemental stresses contribute back to nodal equilibrium through the assembly of internal forces [32]. This deformation-driven information flow provides the physical basis for the proposed finite-element-inspired bipartite graph formulation.

In this work, we develop a cross-attention-based bipartite graph neural network, denoted as CAtt-BiGNN, for coupled prediction of nodal and elemental fields in sheet material forming. The graph contains two types of vertices: mesh-node vertices, which carry nodal kinematic and contact-related information, and element vertices, which carry element-level deformation information. Directed node–element edges encode local geometric relations and provide the communication pathway between the two domains. This construction is finite-element-inspired in the sense that it follows the native node–element structure of the discretisation, but the model remains a learned surrogate rather than an explicitly constrained finite-element solver.

The proposed architecture is designed around four modelling choices. First, the bipartite graph representation reduces the need to interpolate element-level targets from node-only predictions. Second, an edge-aware cross-attention processor learns adaptive weights for node–element message passing, using geometric edge information to modulate the coupling between nodal and elemental states. While the module follows the query–key principle

of cross-attention [33], its attention scores are conditioned on finite-element edge attributes, distinguishing it from standard Transformer attention and conventional graph attention mechanisms [34]. Third, a hierarchical extension, CAtt-BiUGNN, introduces downsampling and upsampling operations to improve information propagation on larger forming meshes. Finally, an adaptive Gaussian noise strategy is evaluated as a rollout-stabilisation technique for autoregressive prediction.

The proposed model is evaluated using sheet material forming simulations. Sheet material forming is widely used in the production of lightweight and high-strength components for automotive, aerospace, and energy applications [35]. Manufacturability assessment relies on accurate prediction of displacement fields, strain localisation, and thickness variation, as these quantities indicate the likelihood of defects such as wrinkling or fracture [36, 37]. In this context, CAtt-BiGNN predicts nodal displacement fields and elemental thinning fields. The contributions of this work are summarised as follows.

- A finite-element-inspired bipartite graph representation is introduced to retain nodal and elemental quantities on their native discretisation domains, allowing nodal displacement increments and elemental thinning values to be predicted without node–element interpolation.
- An edge-aware cross-attention processor is developed to model directional node–element interactions. Unlike standard graph attention or conventional cross-attention, the attention keys are constructed from geometric edge embeddings, enabling the message weights to depend on local node–element relations.
- A hierarchical CAtt-BiUGNN extension is proposed to improve information propagation on larger forming meshes through downsampling, upsampling, and skip connections while preserving the same bipartite node–element formulation.
- An adaptive noise training strategy is designed to enhance the stability of autoregressive rollout and reduce error accumulation in dynamic forming simulations.
- The model is evaluated through controlled ablation studies on cold- and hot-forming benchmarks, showing consistent improvements in both

nodal displacement prediction and elemental thinning prediction during autoregressive rollout.

The remainder of the paper is organised as follows. Section 2 reviews the node–element transfer pattern in the explicit finite element formulation and defines the surrogate prediction problem. Section 3 provides an overview of the proposed CAtt-BiGNN framework and its hierarchical extension. Section 4 describes the dataset generation procedure for the benchmark forming cases. Sections 5 and 6 present the bipartite graph representation and the proposed cross-attention-based bipartite graph neural network. Section 7 details the training, rollout, and adaptive Gaussian noise settings. Section 8 evaluates the proposed modelling choices through numerical comparisons and ablation studies, and Section 9 concludes the paper.

2. Explicit dynamic FE formulation and problem definition

Before introducing the bipartite graph representation in Section 5 and the model design in Section 6, this section reviews the explicit finite element (FE) update cycle that motivates the proposed graph-based design. The review focuses on the node–element information flow relevant to the surrogate model: nodal forces determine nodal accelerations and displacement increments; nodal displacement increments are transferred to elements to update strain, stress, and thickness-related quantities; and updated elemental stresses are then assembled back into nodal internal forces for the next explicit step.

The following notation is used throughout this section. The position of node v at time t^n is denoted by \mathbf{x}_v^n , and its reference position is \mathbf{x}_v^0 . The accumulated nodal displacement and one-step displacement increment are defined as

$$\mathbf{u}_v^n = \mathbf{x}_v^n - \mathbf{x}_v^0, \quad \Delta \mathbf{u}_v^{n+1} = \mathbf{u}_v^{n+1} - \mathbf{u}_v^n = \mathbf{x}_v^{n+1} - \mathbf{x}_v^n. \quad (1)$$

Global vectors are written without the node subscript, for example \mathbf{u}^n and $\Delta \mathbf{u}^{n+1}$. The element index is denoted by i , and the integration-point index within element i is denoted by q . This distinction is important because stresses, strains, and thickness variables are generally evaluated at integration points, whereas the graph model later uses an element-level representation of these quantities.

2.1. Governing equation and explicit time integration

In sheet-material-forming applications, explicit dynamic integration is commonly used because it avoids the repeated global nonlinear solves required by implicit methods and can handle complex tool-blank contact efficiently [38, 39, 32]. Time is discretised as $t^n = n \Delta t$, where Δt is the time increment. Quantities evaluated at t^n are denoted by the superscript n , and half-step velocities are denoted by $n \pm \frac{1}{2}$.

The semi-discrete nodal equilibrium equation at timestep n is written as

$$\mathbf{M} \ddot{\mathbf{u}}^n = \mathbf{P}_{\text{ext}}^n - \mathbf{I}_{\text{int}}^n, \quad (2)$$

where \mathbf{M} is the lumped mass matrix, $\ddot{\mathbf{u}}^n$ is the nodal acceleration vector, $\mathbf{P}_{\text{ext}}^n$ is the external nodal force vector, and $\mathbf{I}_{\text{int}}^n$ is the internal nodal force vector assembled from elemental stress contributions. In forming simulations, $\mathbf{P}_{\text{ext}}^n$ is dominated by tool-blank contact forces, while $\mathbf{I}_{\text{int}}^n$ depends on the current elemental stress state.

Equation (2) gives the acceleration at the current timestep after the external and internal forces have been evaluated. The acceleration is therefore not known a priori for the whole trajectory: it changes with the evolving geometry, contact state, strain, stress, and thickness-related elemental states. The displacement field must consequently be advanced step by step through the explicit time-integration scheme.

2.2. Nodal kinematics and node-to-element strain transfer

2.2.1. Nodal kinematics update

Given the nodal acceleration from Eq. (2), the central-difference scheme updates the half-step velocity as

$$\dot{\mathbf{u}}^{n+\frac{1}{2}} = \dot{\mathbf{u}}^{n-\frac{1}{2}} + \ddot{\mathbf{u}}^n \Delta t, \quad (3)$$

$$\dot{\mathbf{u}}^{1/2} = \dot{\mathbf{u}}^0 + \frac{1}{2} \ddot{\mathbf{u}}^0 \Delta t \quad \text{for the first step.} \quad (4)$$

Here, $\dot{\mathbf{u}}^{n \pm \frac{1}{2}}$ denotes the nodal velocity at the half timesteps. If the blank starts from rest, $\dot{\mathbf{u}}^0 = \mathbf{0}$, so the first-step velocity becomes $\dot{\mathbf{u}}^{1/2} = \frac{1}{2} \ddot{\mathbf{u}}^0 \Delta t$.

The displacement increment over the interval $[t^n, t^{n+1}]$ is then

$$\Delta \mathbf{u}^{n+1} = \dot{\mathbf{u}}^{n+\frac{1}{2}} \Delta t, \quad (5)$$

and the accumulated displacement and current nodal position are updated as

$$\mathbf{u}^{n+1} = \mathbf{u}^n + \Delta \mathbf{u}^{n+1}, \quad (6)$$

$$\mathbf{x}^{n+1} = \mathbf{x}^n + \Delta \mathbf{u}^{n+1}. \quad (7)$$

This convention distinguishes the accumulated displacement \mathbf{u}^{n+1} from the displacement increment $\Delta \mathbf{u}^{n+1}$. In the surrogate formulation introduced later, if the predicted geometry is updated as $\mathbf{x}^{n+1} = \mathbf{x}^n + \Delta \mathbf{u}^{n+1}$ during rollout, then the network output is the displacement increment $\Delta \mathbf{u}^{n+1}$ rather than the accumulated displacement \mathbf{u}^{n+1} .

2.2.2. Node-to-element strain update

After the nodal kinematic update, the displacement information associated with the nodes of each element is transferred to the element integration points. Let $\mathcal{N}(i) = \{v_1, \dots, v_{n_i}\}$ denote the set of nodes connected to element i . If \mathbf{u}^n denotes the global stacked nodal displacement vector, the element-level nodal displacement vector for element i can be extracted through the connectivity as

$$\mathbf{u}_{\mathcal{N}(i)}^n = \mathbf{S}_i \mathbf{u}^n, \quad \Delta \mathbf{u}_{\mathcal{N}(i)}^{n+1} = \mathbf{S}_i \Delta \mathbf{u}^{n+1}, \quad (8)$$

where \mathbf{S}_i is a Boolean extraction matrix that selects the displacement components of the nodes belonging to element i .

At integration point q of element i , the strain and strain increment are obtained from the element nodal displacement vector through the strain-displacement matrix [32]:

$$\boldsymbol{\varepsilon}_{iq}^n = \mathbf{B}_{iq}^n \mathbf{u}_{\mathcal{N}(i)}^n, \quad (9)$$

$$\Delta \boldsymbol{\varepsilon}_{iq}^{n+1} \approx \mathbf{B}_{iq}^n \Delta \mathbf{u}_{\mathcal{N}(i)}^{n+1}. \quad (10)$$

Here, \mathbf{B}_{iq}^n is the strain-displacement matrix evaluated for element i at integration point q , using the configuration at timestep n . It is constructed from the derivatives of the element shape functions with respect to the current or reference coordinates, depending on the adopted finite-strain formulation. Equation (9) connects the strain at integration point q to the displacements of the nodes in $\mathcal{N}(i)$, while Eq. (10) gives the corresponding incremental strain update over $[t^n, t^{n+1}]$.

This transfer is one of the motivations for the bipartite graph representation introduced in Section 5. In the FE formulation, element-level quantities are not obtained from isolated element features; they are computed from the displacements of the connected nodes through element connectivity and shape-function derivatives.

2.3. Constitutive update and thinning evaluation

With the strain increment obtained at each integration point, the material constitutive update gives the stress increment. In compact linearised notation, this can be written as

$$\Delta\boldsymbol{\sigma}_{iq}^{n+1} = \mathbf{C}_{iq}^n \Delta\boldsymbol{\varepsilon}_{iq}^{n+1}, \quad (11)$$

$$\boldsymbol{\sigma}_{iq}^{n+1} = \boldsymbol{\sigma}_{iq}^n + \Delta\boldsymbol{\sigma}_{iq}^{n+1}, \quad (12)$$

where $\boldsymbol{\sigma}_{iq}^n$ is the stress tensor, and \mathbf{C}_{iq}^n is the material tangent or algorithmic material matrix at integration point q of element i . The precise form of \mathbf{C}_{iq}^n depends on the constitutive law and may depend on temperature, strain rate, or other internal variables.

In sheet forming, thickness evolution is an important elemental deformation measure. Let th_{iq}^n be the current thickness associated with integration point q of element i , and let th_{iq}^0 be its initial value. Using the through-thickness logarithmic strain convention [39], the accumulated through-thickness strain is

$$\varepsilon_{33,iq}^n = \ln \left(\frac{\text{th}_{iq}^n}{\text{th}_{iq}^0} \right), \quad \text{th}_{iq}^{n+1} = \text{th}_{iq}^n \exp(\Delta\varepsilon_{33,iq}^{n+1}). \quad (13)$$

Here, the subscript 33 denotes the through-thickness direction in the local sheet coordinate system. In a plane-stress sheet formulation, the thickness-direction strain is treated as a dependent quantity. At each explicit timestep, it is recovered during the constitutive update from the in-plane components of the strain increment $\Delta\boldsymbol{\varepsilon}_{iq}^{n+1}$, together with the plastic incompressibility condition [40]. This connection makes thinning an elemental quantity, rather than a purely nodal quantity.

The thinning ratio is defined as

$$\theta_{iq}^n = 1 - \frac{\text{th}_{iq}^n}{\text{th}_{iq}^0} = 1 - \exp(\varepsilon_{33,iq}^n). \quad (14)$$

Here, $\theta_{iq}^n = 0$ indicates no thickness change, $\theta_{iq}^n > 0$ indicates thinning, and $\theta_{iq}^n < 0$ indicates thickening.

2.4. Element-to-node force assembly and contact update

After the stress field is updated at the integration points, the corresponding elemental internal force contributions are mapped back to the connected nodes. For element i , the elemental internal nodal force vector is obtained from the virtual-work relation as

$$\mathbf{f}_{i,\text{int}}^{n+1} = \int_{\Omega_i^{n+1}} (\mathbf{B}_i^{n+1})^\top \boldsymbol{\sigma}_i^{n+1} d\Omega, \quad (15)$$

where Ω_i^{n+1} is the current domain of element i , $d\Omega$ is the differential measure over that domain, \mathbf{B}_i^{n+1} is the strain–displacement matrix over the element, and $\boldsymbol{\sigma}_i^{n+1}$ is the updated stress field. The transpose of \mathbf{B}_i^{n+1} appears because stresses are mapped to equivalent nodal forces through the virtual-work statement.

In practice, Eq. (15) is evaluated by numerical quadrature. Let $q = 1, \dots, n_q$ index the integration points of element i , where n_q is the number of integration points. The quadrature form is

$$\mathbf{f}_{i,\text{int}}^{n+1} \approx \sum_{q=1}^{n_q} w_q (\mathbf{B}_{iq}^{n+1})^\top \boldsymbol{\sigma}_{iq}^{n+1} J_{iq}^{n+1}. \quad (16)$$

where w_q is the quadrature weight, J_{iq}^{n+1} is the corresponding Jacobian or integration-measure factor, and \mathbf{B}_{iq}^{n+1} and $\boldsymbol{\sigma}_{iq}^{n+1}$ are evaluated at integration point q .

The global internal force vector is then assembled by scattering the elemental contributions into the connected nodal degrees of freedom:

$$\mathbf{I}_{\text{int}}^{n+1} = \sum_{i=1}^{N_e} \mathbf{S}_i^\top \mathbf{f}_{i,\text{int}}^{n+1}. \quad (17)$$

where N_e is the total number of elements. Since \mathbf{S}_i extracts the degrees of freedom associated with element i from the global nodal vector, its transpose \mathbf{S}_i^\top scatters the element-level nodal force vector back into the corresponding entries of the global internal force vector.

In addition to the internal force vector, external nodal forces are evaluated from boundary conditions and tool–blank contact. For each slave node in contact, the contact algorithm evaluates the gap between the blank node and the tool surface, the projected contact point, and the local tool normal. These

quantities determine the direction and magnitude of the contact contribution to $\mathbf{P}_{\text{ext}}^{n+1}$ according to the contact formulation used by the FE solver.

The explicit update cycle is then repeated: contact and other external forces are evaluated, internal forces are assembled from the updated elemental stresses, Eq. (2) gives the next nodal acceleration, and Eqs. (3)–(7) update the nodal kinematics. This cycle creates a bidirectional dependency between nodal and elemental quantities. Nodal displacement increments drive elemental strain, stress, and thinning updates through Eqs. (8)–(10), while elemental stresses are assembled back into nodal internal forces through Eqs. (15)–(17).

The proposed surrogate model does not explicitly solve Eqs. (2)–(17) or enforce stress equilibrium. Instead, the FE formulation is used to identify the native information-transfer structure between nodal kinematics and elemental deformation measures, which is then embedded as an architectural inductive bias.

3. Overview of the proposed CAtt-BiGNN model architecture

Based on the FE derivations established in Section 2, we propose the CAtt-BiGNN model, which is inspired by explicit dynamic FE formulations. A general workflow of its hierarchical extension (CAtt-BiUGNN) is presented in Figure 1. CAtt-BiUGNN retains the same bipartite message-passing scheme as CAtt-BiGNN, while introducing a downsampling and up-sampling mechanism to improve scalability on large, industrial-scale meshes. The workflow begins with the generation of simulation data (Section 4), from which both nodal and elemental states are extracted. These states are then preprocessed into an FE-inspired bipartite graph representation (Section 5). In this representation, nodes and elements are treated as graph entities, while graph edges encode geometric relations. The subsequent step is the model development (Section 6), which follows an encoder–processor–decoder design with skip connections. In this design, message passing is integrated with a cross-attention mechanism to fuse nodal and elemental information across different scales. Once trained, the model performs autoregressive rollout from the undeformed configuration and dynamically recomputes contact features at each predicted timestep to ensure consistency with the evolving geometry. The model directly outputs both nodal kinematics and elemental states such as thinning fields. This removes the need for interpolation and complex post-processing. The model evaluation is presented in Section 8. It assesses field-level accuracy over time using quantitative error metrics, compares the

proposed model with baseline surrogates, and examines robustness during autoregressive rollout across representative forming cases.

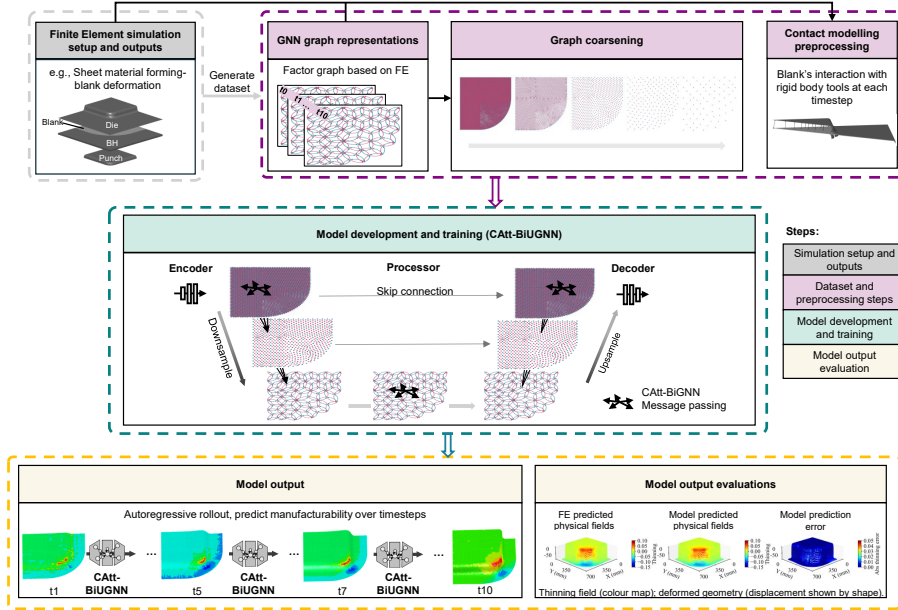


Figure 1: Overview of the proposed workflow.

4. Dataset generation

The FE simulations were recorded at 11 discrete timesteps, following the standard output settings commonly used in commercial sheet-forming solvers. The first timestep corresponds to the undeformed initial configuration, while the remaining ten timesteps describe the progressive deformation of the blank throughout the forming process. Such temporal resolution is typically sufficient to capture the overall deformation evolution and the key stages relevant for manufacturability evaluation and design analysis.

Two benchmark forming scenarios were considered in this study: a dome-shaped case representing cold forming and a corner-shaped case representing hot forming. The corresponding simulation configurations and dataset generation procedures are presented in the following subsections.

4.1. Dome-shaped geometry

The dome-shaped geometry has a double-curvature surface, which leads to a more complex stress and deformation state than single-curvature geometries. For this reason, it is often used as a baseline to evaluate manufacturability [41]. Figure 2 summarises the cold-stamping configuration used in this work. The die, punch, blank holder, and spacers are modelled as rigid bodies, whereas the blank is treated as deformable. The die remains fully constrained. The punch travels vertically at a constant stamping speed of 500 mm/s to draw the blank into the die cavity. To stabilise the flange region and suppress wrinkling, a blank holding force of 200 kN is applied to the blank holder. Spacers of thickness 2.2 mm are inserted between the die and the blank holder to introduce a controlled offset, which promotes more stable material flow. The blank material follows a simplified isotropic constitutive law for cold-work Al2008, taken from the PAM-STAMP material database. The initial blank thickness is 2 mm, and the friction coefficient is set to 0.12.

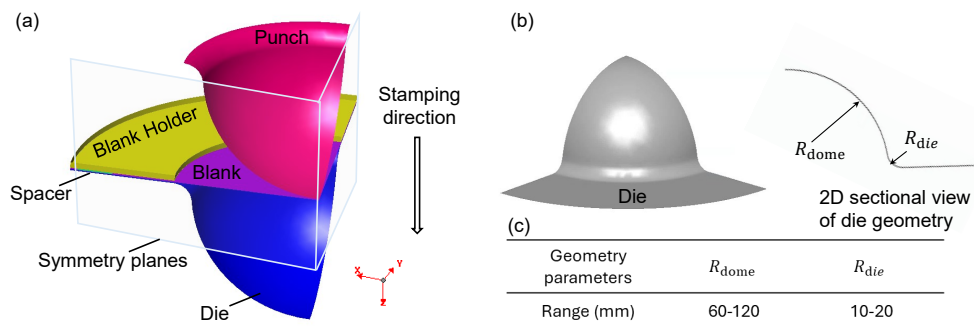


Figure 2: Dome case study (a) simulation setup (b) geometry parameter variables (c) design of experiments

A family of dome-shaped tool geometries is generated using the Design of Experiments (DoE) scheme in Figure 2(c). Two geometric parameters define the die profile: the dome radius R_{dome} and the die radius R_{die} . The DoE ranges are $60 \text{ mm} \leq R_{\text{dome}} \leq 120 \text{ mm}$ and $10 \text{ mm} \leq R_{\text{die}} \leq 20 \text{ mm}$. The punch geometry is constructed by applying a 2 mm offset with respect to the die. To reduce computational cost, only one quarter of the dome is simulated. Symmetry planes are imposed as boundary conditions, and the same uniform quarter-circle blank is used for all cases.

Dataset generation is fully automated and follows the workflow reported in [42]. Latin Hypercube Sampling (LHS) is used to draw tool-parameter

combinations within the prescribed DoE ranges. Training, validation, and test subsets are sampled independently to improve design-space coverage and to reduce the risk of distribution leakage across splits. For each sampled design, tool geometries are created programmatically in SolidWorks, meshed using HyperMesh, and then simulated in PAM-STAMP. The resulting dataset contains 50 training cases, 25 validation cases, and 25 test cases. Each case corresponds to a unique tool configuration and provides stamping outputs over 11 timesteps, which capture the deformation evolution under varying tool geometries.

4.2. Corner-shaped geometry

A hot-formed deep drawn corner case study was considered, as illustrated in Figure 3(c). The die geometry was defined by four design variables: the die corner radius R_{die} , the punch radius R_{punch} , the plan view radius R_{planview} , and the overall height H . The parameter ranges were specified as $25 \text{ mm} \leq R_{\text{die}} \leq 40 \text{ mm}$, $20 \text{ mm} \leq R_{\text{punch}} \leq 27.3 \text{ mm}$, $70 \text{ mm} \leq R_{\text{planview}} \leq 250 \text{ mm}$, and $60 \text{ mm} \leq H \leq 120 \text{ mm}$. The punch geometry was defined with a constant offset of 2.3 mm with respect to the die. For all simulations, the blank shape remained unchanged and a single uniform blank geometry was used across the dataset. The sampling of tool configurations followed a Design of Experiment (DoE) strategy. Parameter combinations were generated using Latin Hypercube Sampling (LHS) within the specified bounds. For each sampled configuration, the CAD model of the tool set was generated automatically. The geometries were subsequently meshed in HyperMesh and then analysed in PAM-STAMP through an automated simulation workflow.

The forming process was modelled using an elastic–viscoplastic constitutive description of AA6082 suitable for hot stamping conditions [42, 43]. The sheet was initially heated to 500 °C, whereas the forming tools were maintained at 25 °C. A stamping velocity of 500 mm/s was applied during forming. The spacer thickness was set to 2.3 mm and the blank thickness was set to 2 mm. To control material flow during forming, a blank holding force of 200 kN was applied through the blank holder in the direction opposite to the stamping motion. In the simulation setup, the punch remained fully constrained while the die translated in the negative z -direction, with the stroke determined by the geometric configuration (total height) of the die.

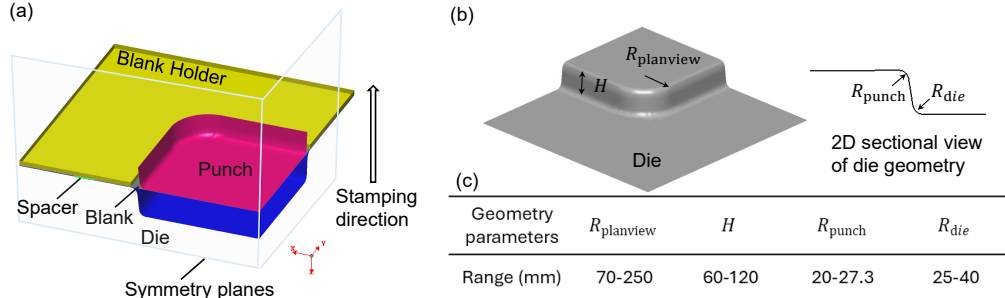


Figure 3: Corner case study (a) simulation setup (b) geometry parameter variables (c) design of experiment

Based on the defined DoE parameter space and process configuration, batch finite element simulations were performed in PAM-STAMP to construct the dataset. Three independent simulation batches were executed, producing 100 training samples, 25 validation samples, and 25 test samples. Each simulation was recorded at 11 discrete timesteps, yielding a temporal sequence that captures the evolution of sheet deformation under different tool geometries.

5. Graph representation and processing

Based on the explicit FE formulation introduced in Section 2, we construct a bipartite graph representation that reflects the bidirectional information exchange between nodal and elemental variables. This bipartite graph representation is shown in Figure 4. Starting from the original FE mesh, two types of graph vertices are defined: mesh nodes, which represent nodal degrees of freedom, and element vertices, which represent element-level states obtained from the corresponding elemental or integration-point quantities. Rather than adopting the original mesh edges as graph connections, the graph is built with bidirectional links between each element and its associated mesh nodes. This construction is motivated by the FE coupling described in Section 2: nodal displacement increments are transferred to elements for strain and thickness-related updates, while elemental stress contributions are assembled back to nodes through the internal force vector.

Following the bipartite graph representation, graph input and output features are defined in Table 1. In the following, a node vertex refers to a

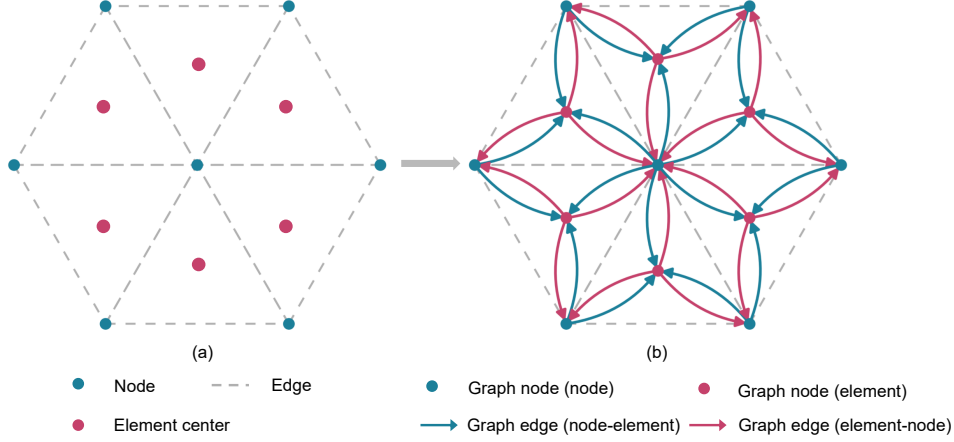


Figure 4: Bipartite graph construction. (a) FE mesh with mesh nodes, FE mesh edges, and element-level quantities located at element centres or representative integration points. (b) Bipartite graph in which mesh-node vertices and element vertices are connected by directed node-to-element and element-to-node edges. Dashed FE mesh edges are shown only to indicate the original mesh connectivity and are not used as graph message-passing edges

mesh node v , and an element vertex refers to a finite element i . The notation is chosen to be consistent with Section 2. The nodal position at timestep n is denoted by \mathbf{x}_v^n , the accumulated nodal displacement by \mathbf{u}_v^n , and the one-step displacement increment by $\Delta \mathbf{u}_v^{n+1}$. The element-level thinning value θ_i^n denotes the thinning value stored for element i in the surrogate dataset. It represents the element-level FE output associated with the integration-point thinning response θ_{iq}^n defined in Eq. (14).

The node input feature vector is constructed in a form motivated by the explicit FE formulation. The nodal displacement-increment input $\Delta \mathbf{u}_v^n$ represents the most recent one-step nodal motion available at timestep n , consistent with the explicit kinematic update in Eq. (5). The boundary indicator \mathbf{b}_v represents fixed degrees of freedom in the three coordinate directions. To incorporate tool-blank contact, the contact-related node feature \mathbf{c}_v^n includes the signed tool-blank gap distance d_v^n from node v to the rigid tool surface and the local tool surface normal \mathbf{n}_v^n . These quantities correspond to the contact update discussed in Section 2.4. The node output is defined as the predicted displacement increment $\Delta \mathbf{u}_v^{n+1}$, which advances the nodal position

through Eq. (7). During autoregressive rollout, the predicted displacement increment is used as the nodal displacement-increment input for the next step, while the updated nodal position \mathbf{x}_v^{n+1} is used to recompute geometry-dependent edge features and contact-related node features. The global input l represents the stroke value that determines the travel distance of the rigid body tools.

Table 1: Input and output features in the bipartite graph representation.

Symbol	Type	Features
$\mathbf{v}_v^n, \mathbf{c}_v^n$	Node input	$\mathbf{v}_v^n = [\Delta \mathbf{u}_v^n, \mathbf{b}_v]$ $\mathbf{b}_v = (b_{v,x}, b_{v,y}, b_{v,z}) \in \{0, 1\}^3$ $\mathbf{c}_v^n = [d_v^n, \mathbf{n}_v^n]$
\mathbf{s}_i^n	Element input	$\mathbf{s}_i^n = \theta_i^n$
l	Global input	$l = \text{stroke}$
$\mathbf{e}_{v \rightarrow i}^n$	Node-to-element edge input	$\mathbf{e}_{v \rightarrow i}^n = [\ \Delta \mathbf{x}_{v,i}^0\ _2, \Delta \mathbf{x}_{v,i}^0, \ \Delta \mathbf{x}_{v,i}^n\ _2, \Delta \mathbf{x}_{v,i}^n]$ $\ \Delta \mathbf{x}_{v,i}^n\ _2 = \sqrt{(\Delta x_{v,i}^n)^2 + (\Delta y_{v,i}^n)^2 + (\Delta z_{v,i}^n)^2}$
$\mathbf{e}_{i \rightarrow v}^n$	Element-to-node edge input	$\mathbf{e}_{i \rightarrow v}^n = [\ \Delta \mathbf{x}_{v,i}^0\ _2, \Delta \mathbf{x}_{v,i}^0, \ \Delta \mathbf{x}_{v,i}^n\ _2, \Delta \mathbf{x}_{v,i}^n]$
$\mathbf{v}_v^{n,\text{out}}$	Node output	$\mathbf{v}_v^{n,\text{out}} = \Delta \mathbf{u}_v^{n+1}$
$\mathbf{s}_i^{n,\text{out}}$	Element output	$\mathbf{s}_i^{n,\text{out}} = \theta_i^{n+1}$

Graph edge input features represent the geometric relation between mesh nodes and their associated elements. For element i , the set of connected nodes is denoted by $\mathcal{N}(i)$, consistent with Section 2.2.2. The element position \mathbf{x}_i^n is taken as the element-centre position at timestep n , and $\Delta \mathbf{x}_{v,i}^n = \mathbf{x}_v^n - \mathbf{x}_i^n$ denotes the node position relative to the element centre. The Euclidean distance $\|\Delta \mathbf{x}_{v,i}^n\|_2$ is rotation-invariant, while the coordinate-difference vector $\Delta \mathbf{x}_{v,i}^n$ retains directional information. The same geometric descriptor is used for both $\mathbf{e}_{v \rightarrow i}^n$ and $\mathbf{e}_{i \rightarrow v}^n$. This is because the descriptor characterises the shared node–element pair geometry rather than a source-to-target direction vector; the two directions of information transfer are distinguished by the corresponding message-passing update. This shared descriptor also allows the two directed edge types to use the same edge-feature initialisation, reducing

parameter count and computational cost. The Reference-configuration edge features at t^0 are included together with the current-configuration features at t^n , so the model receives both a fixed geometric baseline and an updated description of the evolving geometry.

This edge design follows the FE-inspired node–element information flow described in Section 2. In the FE formulation, nodal displacement increments are extracted through the element connectivity and transferred to element integration points, as described by Eqs. (8)–(10). Conversely, elemental stress contributions are assembled back into the global internal force vector through Eq. (17). The bipartite graph does not explicitly evaluate these FE operators, but its two directed edge sets provide a learning structure that reflects the same node-to-element and element-to-node exchange. The use of relative geometric features is also consistent with mesh-based GNN practice [12].

The element input feature is defined as the element-level thinning indicator θ_i^n , corresponding to the thinning definition in Eq. (14). The element output is the predicted thinning value θ_i^{n+1} at the subsequent timestep. In this way, the model learns to predict nodal displacement increments and elemental thinning evolution on their native FE domains, enabling joint prediction of nodal kinematics and element-level deformation behaviour without node–element interpolation.

6. CAtt-BiGNN model development

This section introduces the proposed cross-attention-based bipartite graph neural network, denoted as CAtt-BiGNN, and its hierarchical extension, CAtt-BiUGNN. The graph representation introduced in Section 5 contains two types of graph vertices: mesh-node vertices, which carry nodal kinematic and contact information, and element vertices, which carry element-level deformation information. The model exchanges information between these two domains through directed node-to-element and element-to-node edges. This design follows the node-to-element and element-to-node transfer pattern discussed in Section 2, while remaining a data-driven surrogate rather than an explicit enforcement of the full finite-element equilibrium equations.

To keep the notation consistent with Sections 2 and 5, the nodal position at timestep n is denoted by \mathbf{x}_v^n , the accumulated nodal displacement by \mathbf{u}_v^n , and the one-step displacement increment by $\Delta\mathbf{u}_v^{n+1}$. Following Table 1, the model node output is denoted by $\mathbf{v}_v^{n,\text{out}}$ and corresponds to $\Delta\mathbf{u}_v^{n+1}$, while the model element output is denoted by $\mathbf{s}_i^{n,\text{out}}$ and corresponds to θ_i^{n+1} . A hat

symbol is reserved for latent neural-network representations, such as $\hat{\mathbf{v}}_{v,L}^n$, rather than for the physical graph input or output variables.

6.1. General description of the CAtt-BiGNN architecture

The CAtt-BiGNN follows an encoder–processor–decoder structure, as illustrated in Figure 5. At timestep n , the graph input contains nodal features \mathbf{v}_v^n , contact features \mathbf{c}_v^n , element features \mathbf{s}_i^n , directed node-to-element edge features $\mathbf{e}_{v \rightarrow i}^n$, directed element-to-node edge features $\mathbf{e}_{i \rightarrow v}^n$, and the global stroke input l , as defined in Table 1.

The implementation uses one encoder for nodal features, three tool-specific encoders for contact features, one encoder for element features, one shared encoder for both directed edge types, and one encoder for the global stroke-related feature. The contact feature \mathbf{c}_v^n in Table 1 is implemented as separate die, punch, and blank-holder contact descriptors. Their encoded latent features are denoted by $\hat{\mathbf{c}}_{v,D}^n$, $\hat{\mathbf{c}}_{v,P}^n$, and $\hat{\mathbf{c}}_{v,BH}^n$, respectively. The encoded latent features before the first processor layer are

$$\begin{aligned} \hat{\mathbf{v}}_{v,0}^n &= f_{\text{en}}^v(\mathbf{v}_v^n), & \hat{\mathbf{s}}_{i,0}^n &= f_{\text{en}}^s(\mathbf{s}_i^n), \\ \hat{\mathbf{c}}_{v,D}^n &= f_{\text{en}}^{c,D}(\mathbf{c}_{v,D}^n), & \hat{\mathbf{c}}_{v,P}^n &= f_{\text{en}}^{c,P}(\mathbf{c}_{v,P}^n), \\ \hat{\mathbf{c}}_{v,BH}^n &= f_{\text{en}}^{c,BH}(\mathbf{c}_{v,BH}^n), & \hat{l} &= f_{\text{en}}^g(l), \\ \hat{\mathbf{e}}_{v \rightarrow i,0}^n &= f_{\text{en}}^e(\mathbf{e}_{v \rightarrow i}^n), & \hat{\mathbf{e}}_{i \rightarrow v,0}^n &= f_{\text{en}}^e(\mathbf{e}_{i \rightarrow v}^n). \end{aligned} \tag{18}$$

Here, f_{en}^v , f_{en}^s , $f_{\text{en}}^{c,D}$, $f_{\text{en}}^{c,P}$, $f_{\text{en}}^{c,BH}$, f_{en}^g , and f_{en}^e denote the encoder networks for the mesh-node feature vector, element feature vector, die contact feature vector, punch contact feature vector, blank-holder contact feature vector, global stroke input, and directed edge feature vector, respectively. The notation $\hat{(\cdot)}$ denotes an encoded latent representation. The subscript 0 denotes the latent feature before the first processor layer. The same edge encoder f_{en}^e is applied to both $\mathbf{e}_{v \rightarrow i}^n$ and $\mathbf{e}_{i \rightarrow v}^n$, because the two directed edge inputs use the same node–element pair descriptor defined in Table 1. The direction of information transfer is represented by the corresponding processor update.

After the processor and hierarchical update stages, the final latent node and element states are decoded to the graph outputs defined in Table 1. In the implementation, the node decoder receives the final node latent feature together with the initial encoded node skip feature and the three encoded contact features. The element decoder receives the final element latent feature together with the initial encoded element skip feature. The decoded

outputs are

$$\begin{aligned} \mathbf{v}_v^{n,\text{out}} &= \Delta \mathbf{u}_v^{n+1} = f_{\text{de}}^{\text{node}} \left(\left[\hat{\mathbf{v}}_v^{n,\text{final}}; \hat{\mathbf{v}}_{v,0}^n; \hat{\mathbf{c}}_{v,D}^n; \hat{\mathbf{c}}_{v,P}^n; \hat{\mathbf{c}}_{v,BH}^n \right] \right), \\ \mathbf{s}_i^{n,\text{out}} &= \theta_i^{n+1} = f_{\text{de}}^{\text{elem}} \left(\left[\hat{\mathbf{s}}_i^{n,\text{final}}; \hat{\mathbf{s}}_{i,0}^n \right] \right). \end{aligned} \quad (19)$$

During autoregressive rollout, the decoded node output $\mathbf{v}_v^{n,\text{out}}$ is accumulated to update the nodal displacement and nodal position:

$$\mathbf{u}_v^{n+1} = \mathbf{u}_v^n + \mathbf{v}_v^{n,\text{out}}, \quad \mathbf{x}_v^{n+1} = \mathbf{x}_v^n + \mathbf{v}_v^{n,\text{out}}. \quad (20)$$

The updated nodal positions and element states are then used to construct the graph input for the next rollout timestep. In particular, geometry-dependent edge features and contact descriptors are recomputed from the updated geometry whenever they depend on the current nodal positions.

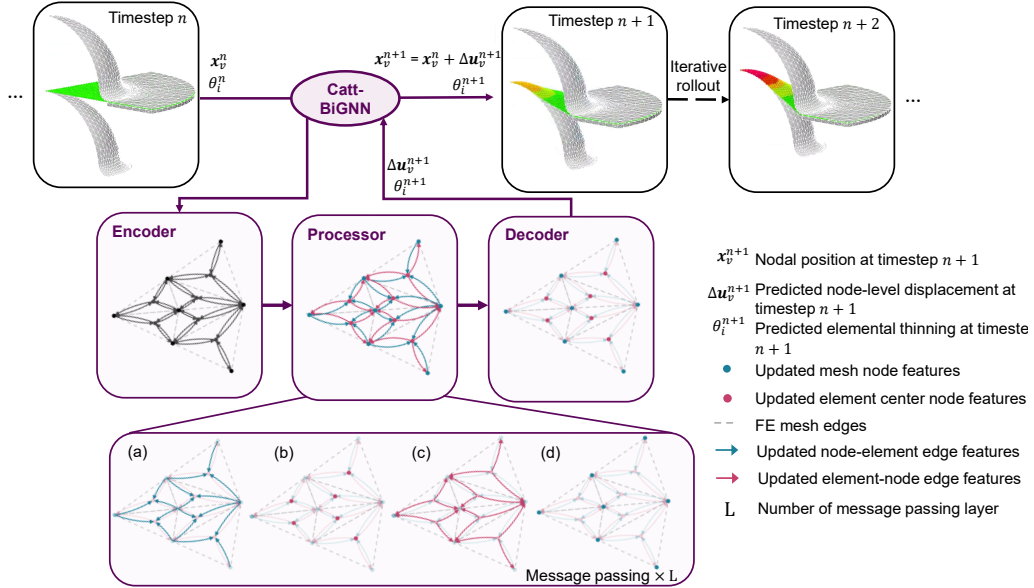


Figure 5: CAtt-BiGNN architecture and autoregressive rollout. At timestep n , the encoded nodal, contact, elemental, and directed edge features are processed by L node–element message-passing layers and decoded into the nodal displacement increment and elemental thinning. The nodal position is updated, and geometry-dependent features are recomputed for the next rollout step. (a)-(d) show the four processor substeps: node-to-element edge update, element update, element-to-node edge update, and mesh-node update.

The processor is the core of the architecture. Each processor layer performs a closed message-passing cycle between nodes and elements. First, node-to-element edge features are updated and aggregated to update the element states. Second, element-to-node edge features are updated and aggregated to update the nodal states. This sequence mirrors the FE-inspired transfer pattern in which nodal kinematic information is used to update element-level quantities, while element-level information is subsequently propagated back to nodal states. The processor is therefore FE-inspired and domain-aligned, but it does not explicitly enforce stress equilibrium or constitutive consistency. A number of processor layers are applied to extend the message-passing range. A tailored cross-attention mechanism is included to enable weighted node–element coupling, as detailed in Section 6.2. The model can operate on a single fine graph and can also be combined with the downsampling and upsampling mechanism described in Section 6.3. When integrated with this multiscale structure, the model forms the hierarchical variant CAtt-BiUGNN.

6.2. Cross-attention-based processor block

The cross-attention-based processor assigns adaptive weights to directed node–element messages. The purpose of the attention mechanism is to let the receiver state decide which incoming geometric relations are most relevant at the current deformation state. In the node-to-element direction, the receiver is an element vertex and the incoming messages originate from connected mesh nodes. In the element-to-node direction, the receiver is a mesh-node vertex and the incoming messages originate from connected elements.

Consistent with Section 5, let $\mathcal{N}(i)$ denote the set of mesh nodes connected to element vertex i . The reverse adjacency set for a mesh node v is denoted by $\mathcal{M}(v) = \{i \mid v \in \mathcal{N}(i)\}$. The corresponding directed edge sets can be written as

$$\mathcal{E}_{\text{in}}^{v \rightarrow i}(i) = \{(v, i) \mid v \in \mathcal{N}(i)\}, \quad \mathcal{E}_{\text{in}}^{i \rightarrow v}(v) = \{(i, v) \mid i \in \mathcal{M}(v)\}. \quad (21)$$

Figure 6 can be read as four steps within one processor layer: (1) update node-to-element edge states, (2) aggregate node-to-element messages and update element states, (3) update element-to-node edge states, and (4) aggregate element-to-node messages and update nodal states. In the attention operation, the receiver state forms the query \mathbf{Q} , the directed edge state forms the key \mathbf{K} , and the updated directed edge state forms the value/message vector \mathbf{V} . This makes the attention weights explicitly edge-aware.

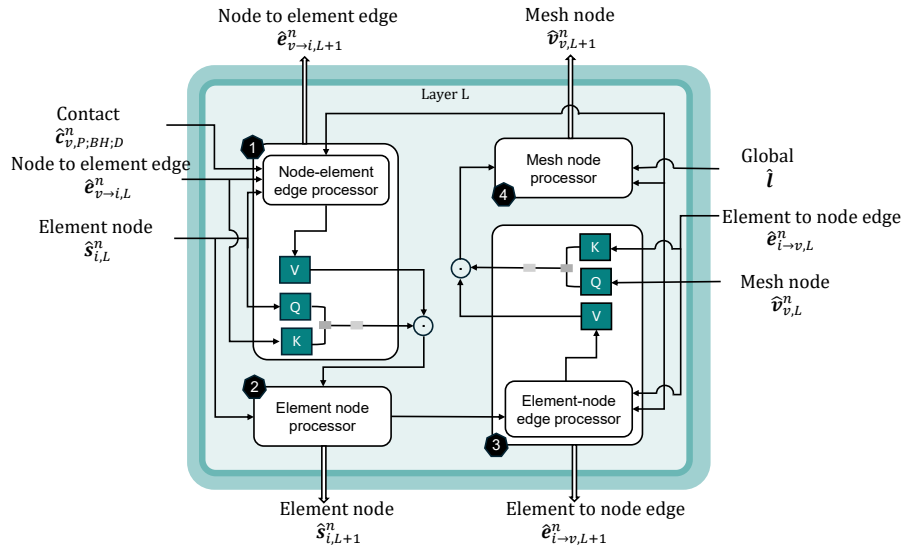


Figure 6: Cross-attention-based CAtt-BiGNN processor block. Each processor layer updates node-to-element edges, element features, element-to-node edges, and mesh-node features in four residual substeps. In the node-to-element update, the receiver element provides the query, while the corresponding edge embedding provides the key and message/value vector; the element-to-node update is defined analogously.

6.2.1. Message passing with attention-modulated aggregation

This subsection describes the data flow within one CAtt-BiGNN processor layer, following the four numbered operations in Figure 6. The message passing layer index is denoted by L , and the timestep index is denoted by n . At the beginning of layer L , $\hat{\mathbf{v}}_{v,L}^n$ denotes the latent feature of mesh node v , $\hat{\mathbf{s}}_{i,L}^n$ denotes the latent feature of element i , $\hat{\mathbf{e}}_{v \rightarrow i,L}^n$ denotes the latent feature of the directed node-to-element edge $v \rightarrow i$, and $\hat{\mathbf{e}}_{i \rightarrow v,L}^n$ denotes the latent feature of the directed element-to-node edge $i \rightarrow v$. The contact latent features of node v are denoted by $\hat{\mathbf{c}}_{v,D}^n$, $\hat{\mathbf{c}}_{v,P}^n$, and $\hat{\mathbf{c}}_{v,BH}^n$, corresponding to the die, punch, and blank-holder contact descriptors.

Step 1: node-to-element edge update. For each directed edge $v \rightarrow i$, the node-to-element edge processor updates the edge latent feature:

$$\hat{\mathbf{e}}_{v \rightarrow i,L+1}^n = \hat{\mathbf{e}}_{v \rightarrow i,L}^n + f_{v \rightarrow i}^e(\hat{\mathbf{v}}_{v,L}^n, \hat{\mathbf{c}}_{v,D}^n, \hat{\mathbf{c}}_{v,P}^n, \hat{\mathbf{c}}_{v,BH}^n, \hat{\mathbf{e}}_{v \rightarrow i,L}^n), \quad (22)$$

where $f_{v \rightarrow i}^e$ is a learnable node-to-element edge-update function. Step 1 produces the updated edge feature $\hat{\mathbf{e}}_{v \rightarrow i,L+1}^n$ and the attention weight $\alpha_{v \rightarrow i,L}^n$. The updated edge feature is used as the node-to-element message,

$$\mathbf{V}_{v \rightarrow i,L}^n = \hat{\mathbf{e}}_{v \rightarrow i,L+1}^n, \quad (23)$$

while $\alpha_{v \rightarrow i,L}^n$ controls the contribution of this message to the receiver element. The computation of $\alpha_{v \rightarrow i,L}^n$ is given in Section 6.2.2.

Step 2: element update. Let $\mathcal{N}(i)$ denote the set of mesh nodes connected to element i . The messages generated in Step 1 are aggregated at element i :

$$\mathbf{m}_{i,L}^{v \rightarrow i,n} = \sum_{v \in \mathcal{N}(i)} \alpha_{v \rightarrow i,L}^n \mathbf{V}_{v \rightarrow i,L}^n. \quad (24)$$

Here, $\mathbf{m}_{i,L}^{v \rightarrow i,n}$ is the aggregated node-to-element message. This message is used to update the element latent feature:

$$\hat{\mathbf{s}}_{i,L+1}^n = \hat{\mathbf{s}}_{i,L}^n + f_{v \rightarrow i}^s(\hat{\mathbf{s}}_{i,L}^n, \mathbf{m}_{i,L}^{v \rightarrow i,n}), \quad (25)$$

where $f_{v \rightarrow i}^s$ is a learnable element-update function. Step 2 produces the updated element feature $\hat{\mathbf{s}}_{i,L+1}^n$, which is then used in the element-to-node edge update.

Step 3: element-to-node edge update. For each directed edge $i \rightarrow v$, the element-to-node edge processor updates the edge latent feature using the updated element feature from Step 2:

$$\hat{\mathbf{e}}_{i \rightarrow v, L+1}^n = \hat{\mathbf{e}}_{i \rightarrow v, L}^n + f_{i \rightarrow v}^e(\hat{\mathbf{s}}_{i, L+1}^n, \hat{\mathbf{v}}_{v, L}^n, \hat{\mathbf{e}}_{i \rightarrow v, L}^n), \quad (26)$$

where $f_{i \rightarrow v}^e$ is a learnable element-to-node edge-update function. Step 3 produces the updated edge feature $\hat{\mathbf{e}}_{i \rightarrow v, L+1}^n$ and the attention weight $\alpha_{i \rightarrow v, L}^n$. The updated edge feature is used as the element-to-node message,

$$\mathbf{V}_{i \rightarrow v, L}^n = \hat{\mathbf{e}}_{i \rightarrow v, L+1}^n, \quad (27)$$

while $\alpha_{i \rightarrow v, L}^n$ controls its contribution to the receiver mesh node. The computation of $\alpha_{i \rightarrow v, L}^n$ is given in Section 6.2.2.

Step 4: mesh-node update. Let $\mathcal{M}(v) = \{i \mid v \in \mathcal{N}(i)\}$ denote the set of elements connected to mesh node v . The messages generated in Step 3 are aggregated at mesh node v :

$$\mathbf{m}_{v, L}^{i \rightarrow v, n} = \sum_{i \in \mathcal{M}(v)} \alpha_{i \rightarrow v, L}^n \mathbf{V}_{i \rightarrow v, L}^n. \quad (28)$$

Here, $\mathbf{m}_{v, L}^{i \rightarrow v, n}$ is the aggregated element-to-node message. This message, together with the encoded global stroke input \hat{l} , is used to update the mesh-node latent feature:

$$\hat{\mathbf{v}}_{v, L+1}^n = \hat{\mathbf{v}}_{v, L}^n + f_{i \rightarrow v}^v(\hat{\mathbf{v}}_{v, L}^n, \mathbf{m}_{v, L}^{i \rightarrow v, n}, \hat{l}), \quad (29)$$

where $f_{i \rightarrow v}^v$ is a learnable mesh-node update function. Step 4 produces the updated mesh-node feature $\hat{\mathbf{v}}_{v, L+1}^n$, completing one bidirectional node–element message-passing layer.

6.2.2. Attention weight computation in CAtt-BiGNN

Section 6.2.1 introduced the attention weights $\alpha_{v \rightarrow i, L}^n$ and $\alpha_{i \rightarrow v, L}^n$, which are generated by the directed edge processors and then used in the element and mesh-node updates. This subsection describes how these weights are computed. The main design choice in CAtt-BiGNN is that the query is constructed from the receiver state, while the key is constructed from the directed edge state. This is because the receiver node or element determines

what information is required, whereas the edge feature carries the local node–element geometric relation. The updated directed edge feature is then used as the value/message vector in the aggregation step.

For clarity, the node-to-element direction is described first. The element-to-node direction follows the same principle with the receiver changed from an element to a mesh node.

Query and key. For a directed edge from mesh node v to element i , the receiver is element i . The query vector is therefore computed from the element latent feature $\hat{\mathbf{s}}_{i,L}^n$:

$$\mathbf{Q}_{i,L}^n = f_q^s(\hat{\mathbf{s}}_{i,L}^n), \quad \mathbf{K}_{v \rightarrow i,L}^n = f_k^s(\hat{\mathbf{e}}_{v \rightarrow i,L}^n). \quad (30)$$

Here, $\mathbf{Q}_{i,L}^n$ is the query vector of element i , and $\mathbf{K}_{v \rightarrow i,L}^n$ is the key vector of the incoming directed edge $v \rightarrow i$. The functions f_q^s and f_k^s are learnable projection functions that map the element latent feature and the directed edge latent feature into the query and key spaces, respectively.

The value/message vector is the updated node-to-element edge feature produced by Step 1 in Section 6.2.1:

$$\mathbf{V}_{v \rightarrow i,L}^n = \hat{\mathbf{e}}_{v \rightarrow i,L+1}^n. \quad (31)$$

No additional value-projection layer is used; the learned edge update itself provides the message to be weighted and aggregated.

Scaled dot-product score. The unnormalised compatibility score for edge $v \rightarrow i$ is computed by a scaled dot product:

$$\rho_{v \rightarrow i,L}^n = \frac{(\mathbf{Q}_{i,L}^n)^\top \mathbf{K}_{v \rightarrow i,L}^n}{\sqrt{d_h}}, \quad (32)$$

where $\rho_{v \rightarrow i,L}^n$ is the unnormalised attention score, and d_h is the hidden dimension of the query and key vectors.

Softmax over incoming edges. For each receiver element i , the softmax is evaluated over all incoming node-to-element edges from the connected node set $\mathcal{N}(i)$:

$$\alpha_{v \rightarrow i,L}^n = \frac{\exp(\rho_{v \rightarrow i,L}^n)}{\sum_{v' \in \mathcal{N}(i)} \exp(\rho_{v' \rightarrow i,L}^n)}. \quad (33)$$

Here, $\alpha_{v \rightarrow i, L}^n$ is the normalised attention weight assigned to the directed edge $v \rightarrow i$. Because the weights are softmax-normalised over the incoming edges of the same receiver element, they satisfy

$$\sum_{v \in \mathcal{N}(i)} \alpha_{v \rightarrow i, L}^n = 1. \quad (34)$$

These weights are then used in Eq. (24) to aggregate the updated node-to-element edge messages.

Element-to-node attention. The element-to-node direction is computed analogously. For a directed edge $i \rightarrow v$, the receiver is mesh node v , so the query is computed from $\hat{\mathbf{v}}_{v, L}^n$, while the key is computed from the directed edge feature $\hat{\mathbf{e}}_{i \rightarrow v, L}^n$:

$$\mathbf{Q}_{v, L}^n = f_q^v(\hat{\mathbf{v}}_{v, L}^n), \quad \mathbf{K}_{i \rightarrow v, L}^n = f_k^v(\hat{\mathbf{e}}_{i \rightarrow v, L}^n), \quad \mathbf{V}_{i \rightarrow v, L}^n = \hat{\mathbf{e}}_{i \rightarrow v, L+1}^n. \quad (35)$$

Here, $\mathbf{Q}_{v, L}^n$ is the query vector of mesh node v , and $\mathbf{K}_{i \rightarrow v, L}^n$ is the key vector of the incoming directed edge $i \rightarrow v$. The functions f_q^v and f_k^v are learnable projection functions that map the mesh-node latent feature and the directed edge latent feature into the query and key spaces, respectively. The corresponding unnormalised score and normalised attention weight are

$$\rho_{i \rightarrow v, L}^n = \frac{(\mathbf{Q}_{v, L}^n)^\top \mathbf{K}_{i \rightarrow v, L}^n}{\sqrt{d_h}}, \quad (36)$$

$$\alpha_{i \rightarrow v, L}^n = \frac{\exp(\rho_{i \rightarrow v, L}^n)}{\sum_{i' \in \mathcal{M}(v)} \exp(\rho_{i' \rightarrow v, L}^n)}. \quad (37)$$

Here, $\rho_{i \rightarrow v, L}^n$ is the unnormalised attention score, $\mathcal{M}(v) = \{i \mid v \in \mathcal{N}(i)\}$ is the set of elements connected to mesh node v . The resulting weights $\alpha_{i \rightarrow v, L}^n$ are used in Eq. (28) to aggregate the updated element-to-node edge messages.

Overall, this attention design makes the node–element coupling edge-aware. The receiver state determines the query, the directed edge state determines the key, and the updated directed edge feature provides the message being weighted. This allows the processor to adapt the strength of node–element information exchange according to the local geometric relation encoded on each edge.

6.3. Downsampling and upsampling mechanism

For larger sheet-forming meshes, applying many CAtt-BiGNN processor layers directly on the finest graph can be computationally expensive and may limit the effective receptive field. To address this, the proposed model is extended to a hierarchical architecture, denoted as CAtt-BiUGNN. As shown in Figure 7, the model first applies CAtt-BiGNN processor layers on the original fine graph, then transfers the mesh-node and element-vertex latent features to coarser graph levels, applies additional CAtt-BiGNN processor layers at the coarsest level, and finally upsamples the features back to the fine graph before decoding.

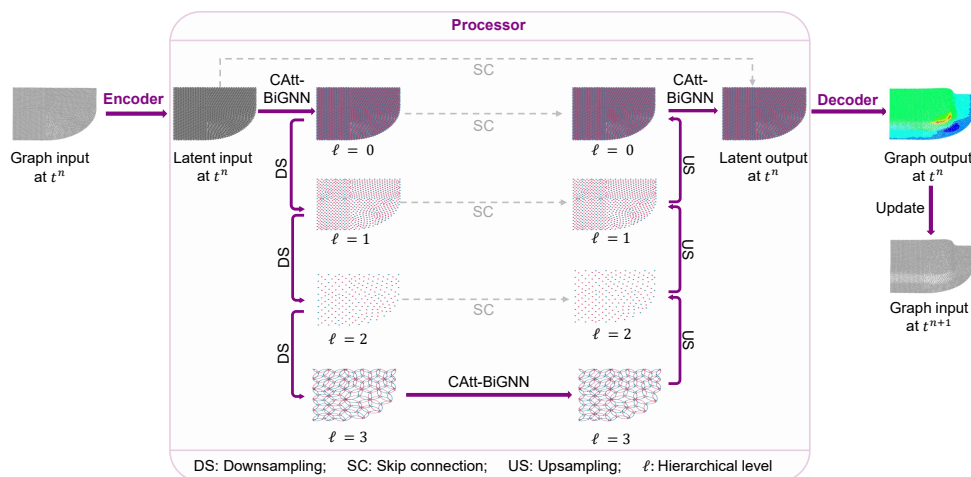


Figure 7: Hierarchical CAtt-BiUGNN architecture. The original fine bipartite graph is encoded and progressively downsampled to coarser graph levels. CAtt-BiGNN processor blocks operate within the hierarchy, while skip connections preserve intermediate latent features. Upsampling transfers the updated coarse-level information back to the fine graph before decoding the nodal displacement increments and elemental thinning values.

The graph hierarchy is indexed by $\ell = 0, 1, \dots, L_g$, where $\ell = 0$ denotes the original fine graph and $\ell = L_g$ denotes the coarsest graph. The timestep index is denoted by n . Superscript V denotes quantities associated with mesh-node vertices, and superscript S denotes quantities associated with element vertices. The symbols \downarrow and \uparrow denote downsampling and upsampling operations, respectively. Mesh-node vertices are indexed by v on level ℓ and by u on level $\ell + 1$. Element vertices are indexed by i on level ℓ and by j on level $\ell + 1$.

Coarsening is applied separately to mesh-node vertices and element vertices. At each selected graph level, the corresponding mesh-node and element-vertex sets form a bipartite graph, so the CAtt-BiGNN processor can be applied. In the corner-shaped case study, three coarsening operations are used, producing four graph levels including the original fine graph, as illustrated in Figure 8.

Inter-level edges define how information is transferred between adjacent graph levels. A KD-tree nearest-neighbour search is used to construct sparse inter-level mappings. The number of nearest neighbours used in the hierarchy is denoted by K_{nn} . In the implementation, each fine-level vertex is connected to its K_{nn} nearest coarse-level vertices.

For downsampling from level ℓ to level $\ell + 1$, let $\mathcal{E}_{\downarrow,\ell}^V$ denote the set of inter-level mesh-node edges from fine mesh nodes to coarse mesh nodes, and let $\mathcal{E}_{\downarrow,\ell}^S$ denote the set of inter-level element-vertex edges from fine element vertices to coarse element vertices. For a coarse mesh node u and a coarse element vertex j , the incoming fine-level neighbour sets are

$$\mathcal{N}_{\downarrow}^V(u) = \{v \mid (v, u) \in \mathcal{E}_{\downarrow,\ell}^V\}, \quad (38)$$

$$\mathcal{N}_{\downarrow}^S(j) = \{i \mid (i, j) \in \mathcal{E}_{\downarrow,\ell}^S\}. \quad (39)$$

Here, $\mathcal{N}_{\downarrow}^V(u)$ is the set of fine-level mesh nodes connected to coarse mesh node u , and $\mathcal{N}_{\downarrow}^S(j)$ is the set of fine-level element vertices connected to coarse element vertex j .

The downsampling operation is applied separately to mesh-node and element-vertex latent features. Let $\hat{\mathbf{v}}_{v,\ell}^n$ denote the latent feature of fine-level mesh node v , and let $\hat{\mathbf{v}}_{u,\ell+1}^n$ denote the resulting latent feature of coarse mesh node u . Similarly, let $\hat{\mathbf{s}}_{i,\ell}^n$ denote the latent feature of fine-level element vertex i , and let $\hat{\mathbf{s}}_{j,\ell+1}^n$ denote the resulting latent feature of coarse element vertex j . The two downsampling operations are

$$\hat{\mathbf{v}}_{u,\ell+1}^n = \phi \left(\mathbf{a}_{\downarrow,\ell}^V + \sum_{v \in \mathcal{N}_{\downarrow}^V(u)} \mathbf{W}_{v \rightarrow u,\ell}^{\downarrow,V} \hat{\mathbf{v}}_{v,\ell}^n \right), \quad (40)$$

$$\hat{\mathbf{s}}_{j,\ell+1}^n = \phi \left(\mathbf{a}_{\downarrow,\ell}^S + \sum_{i \in \mathcal{N}_{\downarrow}^S(j)} \mathbf{W}_{i \rightarrow j,\ell}^{\downarrow,S} \hat{\mathbf{s}}_{i,\ell}^n \right). \quad (41)$$

Here, $\mathbf{W}_{v \rightarrow u,\ell}^{\downarrow,V}$ is the learnable edge-specific weight matrix for the mesh-node inter-level edge (v, u) , and $\mathbf{W}_{i \rightarrow j,\ell}^{\downarrow,S}$ is the corresponding edge-specific weight

matrix for the element inter-level edge (i, j) . The vectors $\mathbf{a}_{\downarrow, \ell}^V$ and $\mathbf{a}_{\downarrow, \ell}^S$ are learnable bias vectors for mesh-node and element-vertex downsampling, respectively. The activation function is denoted by $\phi(\cdot)$.

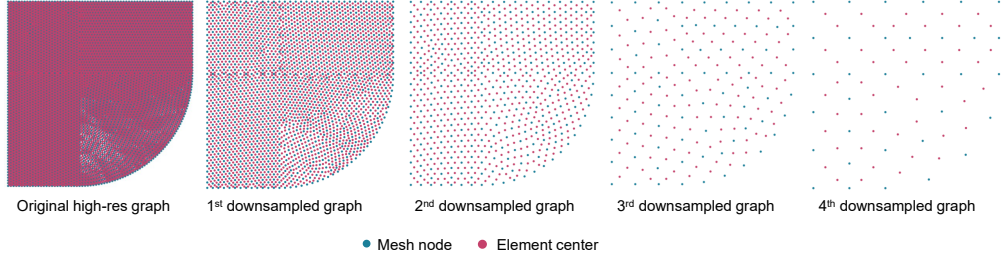


Figure 8: Graph coarsening used for the downsampling and upsampling operations in the corner-shaped case study. Mesh-node vertices and element vertices are coarsened separately. Inter-level edges connect adjacent graph levels using a KD-tree-based nearest-neighbour mapping.

Upsampling transfers the updated coarse-level features back to finer graph levels. The upsampling edge sets are the reverse of the corresponding downsampling mappings. For upsampling from level $\ell + 1$ back to level ℓ , let $\mathcal{E}_{\uparrow, \ell}^V$ denote the set of inter-level mesh-node edges from coarse mesh nodes to fine mesh nodes, and let $\mathcal{E}_{\uparrow, \ell}^S$ denote the set of inter-level element-vertex edges from coarse element vertices to fine element vertices. For a fine mesh node v and a fine element vertex i , the connected coarse-level neighbour sets are

$$\mathcal{N}_{\uparrow}^V(v) = \{u \mid (u, v) \in \mathcal{E}_{\uparrow, \ell}^V\}, \quad (42)$$

$$\mathcal{N}_{\uparrow}^S(i) = \{j \mid (j, i) \in \mathcal{E}_{\uparrow, \ell}^S\}. \quad (43)$$

Here, $\mathcal{N}_{\uparrow}^V(v)$ is the set of coarse mesh nodes connected to fine mesh node v , and $\mathcal{N}_{\uparrow}^S(i)$ is the set of coarse element vertices connected to fine element vertex i .

Skip connections are used during upsampling to preserve features from the corresponding downsampling stage. Let $\hat{\mathbf{v}}_{u, \ell+1}^{n, \text{up}}$ denote the updated coarse mesh-node feature propagated from the coarser part of the network, and let $\hat{\mathbf{v}}_{u, \ell+1}^{n, \text{skip}}$ denote the stored coarse mesh-node feature from the corresponding downsampling stage. Similarly, let $\hat{\mathbf{s}}_{j, \ell+1}^{n, \text{up}}$ and $\hat{\mathbf{s}}_{j, \ell+1}^{n, \text{skip}}$ denote the updated and

stored coarse element features. The two upsampling operations are

$$\hat{\mathbf{v}}_{v,\ell}^{n,\text{up}} = \phi \left(\mathbf{a}_{\uparrow,\ell}^V + \sum_{u \in \mathcal{N}_{\uparrow}^V(v)} \mathbf{W}_{u \rightarrow v,\ell}^{\uparrow,V} \left[\hat{\mathbf{v}}_{u,\ell+1}^{n,\text{up}} ; \hat{\mathbf{v}}_{u,\ell+1}^{n,\text{skip}} \right] \right), \quad (44)$$

$$\hat{\mathbf{s}}_{i,\ell}^{n,\text{up}} = \phi \left(\mathbf{a}_{\uparrow,\ell}^S + \sum_{j \in \mathcal{N}_{\uparrow}^S(i)} \mathbf{W}_{j \rightarrow i,\ell}^{\uparrow,S} \left[\hat{\mathbf{s}}_{j,\ell+1}^{n,\text{up}} ; \hat{\mathbf{s}}_{j,\ell+1}^{n,\text{skip}} \right] \right). \quad (45)$$

Here, $[\cdot; \cdot]$ denotes feature concatenation. The matrices $\mathbf{W}_{u \rightarrow v,\ell}^{\uparrow,V}$ and $\mathbf{W}_{j \rightarrow i,\ell}^{\uparrow,S}$ are learnable edge-specific weight matrices for mesh-node and element-vertex upsampling, respectively. The vectors $\mathbf{a}_{\uparrow,\ell}^V$ and $\mathbf{a}_{\uparrow,\ell}^S$ are the corresponding bias vectors.

After the final upsampling operation returns information to the original fine graph, the resulting fine-level mesh-node and element latent features are passed to the decoder described in Section 6.1. The hierarchical architecture therefore combines local node–element coupling on the fine graph with longer-range information propagation through coarser graph levels.

7. Model training

7.1. Training setup

The models were trained on different computing platforms depending on the case study. For the dome-shaped case study, which contains fewer mesh nodes and elements, training was performed on a workstation equipped with an NVIDIA Quadro 5000 GPU with 16 GB of GPU memory. For the corner-shaped case study, training was conducted on Google Colab using an L4 GPU with 22.5 GB of GPU memory. The dome-shaped case study was trained for 1000 epochs, while the corner-shaped case study was trained for 500 epochs.

All models were trained using the Adam optimiser. The learning rate followed an exponential decay schedule from 10^{-4} to 10^{-6} , consistent with the baseline architectures [12, 21]. Standardisation was applied to the input and output fields before training to improve numerical conditioning and stabilise convergence. The hidden feature dimension was set according to the corresponding model configuration. For the dome-shaped case study, no downsampling or upsampling was used in the architecture, giving a direct comparison between CAtt-BiGNN and conventional mesh-based GNN baselines. The dome model used 20 message-passing layers. For the larger

corner-shaped case study, hierarchical graph downsampling and upsampling were incorporated, as described in Section 6.3, to enable information propagation over longer spatial distances. Following the baseline configuration [21], the hierarchical model used 2 message-passing layers at the finest graph scale and 10 message-passing layers at the coarsest scale.

The training strategy used teacher forcing. At each prediction transition from t^n to t^{n+1} , the ground-truth graph state at t^n was used as the model input, and the model was trained to predict the next-step nodal displacement increments and elemental thinning value, consistent with the graph-output convention defined in Table 1 and the decoder formulation in Section 6.1. During autoregressive validation and testing, the predicted displacement increment was accumulated to update the nodal position, and the updated geometry was then used to recompute geometry-dependent edge features and contact-related node features for the next timestep.

The total training loss combines the nodal displacement increment loss and the elemental thinning loss. Let M denote the number of trajectories, N_p the number of prediction transitions per trajectory, V the number of mesh nodes, and N_e the number of elements. If 11 states are recorded for one rollout, then $N_p = 10$ prediction transitions. A superscript star denotes the FE reference value, while quantities without a star denote model predictions. In the implementation, the losses are evaluated in the standardised output space; the symbol $\widetilde{(\cdot)}$ denotes the corresponding standardised quantity.

The displacement increment loss is

$$\mathcal{L}_{\text{disp}} = \frac{1}{3MN_pV} \sum_{m=1}^M \sum_{n=0}^{N_p-1} \sum_{v=1}^V \sum_{d \in \{x,y,z\}} \left(\widetilde{\Delta u_{v,d}^{m,n+1}} - \widetilde{\Delta u_{v,d}^{*m,n+1}} \right)^2. \quad (46)$$

Here, $\Delta u_{v,d}^{m,n+1}$ is the predicted displacement increment of node v in Cartesian direction d for trajectory m , and $\Delta u_{v,d}^{*m,n+1}$ is the corresponding FE reference increment. This definition follows the rollout update in which the predicted increment, rather than the accumulated displacement, advances the nodal position.

The thinning loss is

$$\mathcal{L}_{\text{thin}} = \frac{1}{MN_pN_e} \sum_{m=1}^M \sum_{n=0}^{N_p-1} \sum_{i=1}^{N_e} \left(\widetilde{\theta_i^{m,n+1}} - \widetilde{\theta_i^{*m,n+1}} \right)^2, \quad (47)$$

where $\theta_i^{m,n+1}$ and $\theta_i^{*m,n+1}$ are the predicted and FE reference elemental thinning values for element i , respectively. The total loss is the unweighted sum of the two terms:

$$\mathcal{L}_{\text{total}} = \mathcal{L}_{\text{disp}} + \mathcal{L}_{\text{thin}}. \quad (48)$$

For evaluation and visualisation, the predicted outputs were transformed back from the standardised space to their original physical units before computing the reported physical error metrics.

7.2. Noise injection

When enabled, adaptive Gaussian noise is used as an optional training robustness strategy for autoregressive rollout, rather than as a change to the CAtt-BiGNN or CAtt-BiUGNN architecture itself. The primary architecture-comparison experiments are therefore conducted without noise injection. This setting allows the predictive capacity of different graph architectures to be compared without introducing model-specific noise perturbation tuning. The effect of noise injection is analysed separately using CAtt-BiUGNN as the reference architecture.

The purpose of noise injection is to reduce the train–test mismatch between teacher-forced training and autoregressive rollout. In teacher forcing, the model receives the ground-truth graph state at timestep n . In autoregressive rollout, the graph state at the next timestep is constructed from previously predicted outputs. Small errors in the predicted displacement increment $\Delta \mathbf{u}_v^{n+1}$ can therefore accumulate through the nodal position update and affect the recomputed edge and contact descriptors at later timesteps. In this work, the perturbation is introduced only during teacher-forced training and is applied to the nodal displacement-increment input. Its direct role is to improve the robustness of the kinematic rollout, while any influence on elemental thinning prediction occurs indirectly through the learned node–element coupling.

A commonly used approach is to add zero-mean Gaussian noise with the same scale to all nodal displacement-increment inputs. However, sheet-forming deformation is spatially nonuniform. In forming simulations, nodes in freely deforming areas undergo large displacements, whereas nodes near contact regions may move only slightly but play a dominant role in determining contact forces. The contact features used in our model include inverse-distance terms, which are sensitive when nodes are close to tooling surfaces. Small geometric fluctuations around these near-contact regions can

significantly change the contact evaluation. Such errors are amplified during autoregressive rollout because contact descriptors are recomputed from the previously predicted geometry. As a result, uniform Gaussian noise does not adequately reflect this effect in sheet material forming.

To account for this behaviour, the adaptive strategy perturbs the nodal displacement increment $\Delta \mathbf{u}_v^n$ inside the node input feature. The perturbation magnitude is scaled by the inverse displacement-increment magnitude of each node. For node v , the inverse-displacement-increment weight is first computed as

$$\gamma_v^n = \frac{1}{\|\Delta \mathbf{u}_v^n\|_2 + \epsilon}, \quad (49)$$

where ϵ is a small positive constant used to avoid division by zero. The weights are then normalised over the mesh-node set \mathcal{V} :

$$\bar{\gamma}_v^n = \frac{\gamma_v^n}{\max_{v' \in \mathcal{V}} \gamma_{v'}^n}. \quad (50)$$

Here, $\bar{\gamma}_v^n \in [0, 1]$ is the adaptive node-wise noise weight. Nodes with smaller displacement-increment magnitudes receive larger weights, while nodes with larger displacement-increment magnitudes receive smaller weights. This gives larger perturbations to slowly moving and contact-sensitive regions, while avoiding excessive perturbation in regions that already undergo large deformation.

The noisy displacement increment used in the node input is then

$$\Delta \mathbf{u}_{v,\text{noise}}^n = \Delta \mathbf{u}_v^n + \bar{\gamma}_v^n \lambda_{\text{noise}} s_{\Delta \mathbf{u}}^n \boldsymbol{\eta}_v^n, \quad \boldsymbol{\eta}_v^n \sim \mathcal{N}(\mathbf{0}, \mathbf{I}_3), \quad (51)$$

where $s_{\Delta \mathbf{u}}^n$ is the scalar standard deviation of the nodal displacement-increment field, λ_{noise} is a manually tuned global noise-scale factor, and \mathbf{I}_3 is the 3×3 identity matrix. The scale factor λ_{noise} controls the overall strength of the injected perturbation and is selected through validation experiments, rather than being learned by the model. The test set is not used to choose λ_{noise} or any other noise parameter.

During training, only the nodal displacement-increment component of the node input is perturbed. The remaining node, element, edge, contact, and global features are kept unchanged for the same teacher-forced sample, and the training targets remain the original FE-computed displacement increment and elemental thinning value at the next timestep.

During autoregressive rollout, no artificial noise is added. The predicted displacement increment is accumulated to update the nodal position, and the contact-related node features and geometry-dependent edge features are recomputed from the updated predicted geometry, as described in Sections 5 and 6.1.

8. Model performance evaluation

The evaluation is organised to test the modelling choices introduced in the previous sections. The dome-shaped case study uses a smaller graph and is used to isolate the effects of the bipartite node–element representation and the edge-aware attention mechanism without hierarchical downsampling and upsampling. The corner-shaped case study uses a larger graph and evaluates the hierarchical CAtt-BiUGNN architecture.

8.1. Dome-shaped case study

Baseline models. The dome-shaped case study involves relatively small graphs. Therefore, no downsampling or upsampling mechanism is used, allowing the comparison to focus on the bipartite representation and attention mechanism. Six model configurations are evaluated, including: (a) MeshGraphNet (MGN), a widely used GNN-based surrogate model for physical simulations, which performs message passing directly on the original mesh [12]. (b) Recurrent GNN (RGNN), MGN with recurrent updates to better capture temporal dependencies [23]. (c) Vanilla-BiGNN, our BiGNN variant that includes bipartite graph construction but does not apply any attention-based aggregation functions. (d) GAT-BiGNN, BiGNN with GAT-based attention aggregation. (e) CA-BiGNN, BiGNN with pure cross-attention-based aggregation. (f) Our proposed CAtt-BiGNN model, which incorporates the designed edge-based cross-attention aggregation described in Section 6.1. Specifically, the main difference between CA-BiGNN and our proposed CAtt-BiGNN is that CA-BiGNN uses the source node or element features to compute the Key matrix, whereas our CAtt-BiGNN model uses edge features to compute the Key matrix.

Among all of the comparative models, MGN and RGNN are treated as external baselines, Vanilla-BiGNN, and GAT-BiGNN, CA-BiGNN are treated as ablation models. All models use the recommended hyperparameters from the baseline configurations [12, 23] and the same GPU setup described in Section 7. Table 2 summarises the comparison results.

Evaluation metrics. Each simulation is evaluated over $N_p = 10$ autoregressive rollout transitions. Following the notation in Section 7, quantities without a superscript star denote model predictions, whereas a superscript star denotes the FE reference. All reported errors are computed after transforming the model outputs back to their original physical units.

Let $\mathbf{x}_v^{N_p}$ and $\mathbf{x}_v^{*N_p}$ denote the predicted and FE reference final nodal positions of mesh node v , respectively. The mean positional Euclidean error is defined as

$$E_{\text{pos}} = \frac{1}{|\mathcal{V}|} \sum_{v \in \mathcal{V}} \|\mathbf{x}_v^{N_p} - \mathbf{x}_v^{*N_p}\|_2, \quad (52)$$

where \mathcal{V} is the mesh-node set. The position mean absolute error (MAE) is

$$E_{\text{MAE}} = \frac{1}{3|\mathcal{V}|} \sum_{v \in \mathcal{V}} \sum_{d=1}^3 |x_{v,d}^{N_p} - x_{v,d}^{*N_p}|. \quad (53)$$

For thinning evaluation, let $\theta_i^{N_p}$ and $\theta_i^{*N_p}$ denote the predicted and FE reference thinning values of element i at the final rollout timestep. The thresholded thinning error is evaluated over

$$\mathcal{T}_\tau = \left\{ i \in \mathcal{S} \mid \left| \theta_i^{*N_p} \right| > \tau \right\}, \quad (54)$$

where \mathcal{S} is the element set and $\tau = 0.005$. The corresponding thinning error is

$$E_{\theta,\tau} = \frac{1}{|\mathcal{T}_\tau|} \sum_{i \in \mathcal{T}_\tau} \left| \theta_i^{N_p} - \theta_i^{*N_p} \right|. \quad (55)$$

The centre-of-mass (COM) distance is computed using the top $p\%$ most thinned elements. Let \mathcal{P}_p and \mathcal{P}_p^* denote the predicted and FE reference top- $p\%$ element sets, respectively, and let $\mathbf{x}_{i,c}^{N_p}$ be the final centre position of element i . The COM distance is

$$E_{\text{COM}}^p = \left\| \frac{1}{|\mathcal{P}_p|} \sum_{i \in \mathcal{P}_p} \mathbf{x}_{i,c}^{N_p} - \frac{1}{|\mathcal{P}_p^*|} \sum_{i \in \mathcal{P}_p^*} \mathbf{x}_{i,c}^{*N_p} \right\|_2. \quad (56)$$

The top- $p\%$ relative thinning error is evaluated on the FE reference top- $p\%$ set:

$$E_{\theta,\text{rel}}^p = \frac{100}{|\mathcal{P}_p^*|} \sum_{i \in \mathcal{P}_p^*} \frac{\left| \theta_i^{N_p} - \theta_i^{*N_p} \right|}{\left| \theta_i^{*N_p} \right| + \epsilon}, \quad (57)$$

where ϵ is a small positive constant used to avoid division by zero. In the dome case, $p = 5$; in the corner case, $p = 1$.

Results. Table 2 summarises the dome-case ablation results at the final roll-out timestep. All relative changes are computed with respect to MGN. Vanilla-BiGNN improves the thinning-related metrics relative to MGN, reducing the thresholded thinning error, top-5% COM distance, and top-5% relative thinning error. This supports the representation-level motivation of the paper: when thinning is predicted on element vertices rather than recovered indirectly from node-centred outputs, the elemental field can be represented more naturally. However, Vanilla-BiGNN does not improve the displacement metrics relative to MGN. This may result from the added coupling between the elemental thinning field and the nodal displacement field. The coupling was expected to facilitate joint learning between the nodal and elemental states; however, the model does not fully capture this dependency effectively. Consequently, inaccuracies in the thinning prediction propagate through the coupling and adversely affect the displacement updates.

Compared with MGN, the proposed CAtt-BiGNN reduces the mean positional Euclidean error by 21.7%, the position MAE by 20.5%, the thresholded thinning error by 36.0%, and the top-5% relative thinning error by 53.8%. The top-5% thinning COM distance is also reduced relative to MGN, although Vanilla-BiGNN gives the lowest COM distance among the tested variants. GAT-BiGNN does not consistently improve over Vanilla-BiGNN. CA-BiGNN improves several metrics, indicating that cross-attention can help modulate node–element message passing. The proposed CAtt-BiGNN gives the best overall balance because its attention mechanism uses directed edge features, which encode local geometric relations such as relative position and distance.

Additionally, comparing GAT-BiGNN with Vanilla-BiGNN, the addition of GAT-based attention computation provides a marginal improvement in predictive performance on both displacement and thinning evaluation metrics. The CA-BiGNN model provides slightly better prediction results on both displacement and thinning evaluation metrics compared to Vanilla-BiGNN. This indicates that cross-attention helps to model node–element interactions.

However, CA-BiGNN still underperforms compared with the proposed CAtt-BiGNN. The main reason lies in how attention is constructed. CA-BiGNN follows the conventional cross-attention design, where the Key ma-

Table 2: Ablation study for the dome case study at the final rollout timestep.

Metric	MGN	RGNN	Vanilla-BiGNN	GAT-BiGNN	CA-BiGNN	CAtt-BiGNN (proposed)
Displacement evaluation metrics						
Mean positional	0.8273	0.6745	0.9081	0.8994	0.7430	0.6482
Euclidean error (mm)		(-18.5%)	(+9.8%)	(+8.70%)	(-10.2%)	(-21.7%)
Position MAE (mm)	0.3866	0.3138	0.4166	0.4223	0.3466	0.3076
		(-18.9%)	(+7.77%)	(+9.23%)	(-10.4%)	(-20.5%)
Thinning evaluation metrics						
Threshold-based thinning error	0.0075	0.0061	0.0054	0.0057	0.0053	0.0048
		(-18.7%)	(-28.0%)	(-24.0%)	(-29.3%)	(-36.0%)
Top 5% thinning COM	2.2757	1.9527	1.5379	1.7088	1.7477	1.6302
		(-14.2%)	(-32.4%)	(-24.9%)	(-23.2%)	(-28.4%)
Top 5% relative thinning error	6.10%	4.19%	3.86%	3.83%	3.10%	2.82%
		(-31.3%)	(-36.7%)	(-37.2%)	(-49.2%)	(-53.8%)

* Values in parentheses denote the relative change (%) with respect to the MGN baseline (lower is better).

trix is derived from the source node or element features. In contrast, CAtt-BiGNN computes the Key matrix from edge features. This design choice leads to better performance because edge features provide richer local geometric and deformation information. As a result, the model can adaptively weight element–node messages more effectively.

Figure 9 presents the evolution of Euclidean positional error and threshold-based thinning error over rollout timesteps. Among all models, CAtt-BiGNN already achieves lower errors than both the baseline methods and the vanilla variant, demonstrating the benefit of incorporating cross attention and bipartite graph representations.

Figure 10 shows the visual comparison of predicted and ground-truth fields for the dome-shaped case study. The figure corresponds to the largest-curvature test case, where positional prediction and thinning error are evaluated at the final rollout timestep, representing the post-forming state. Figure 10 provides a qualitative comparison of the final rollout predictions for the dome-shaped case. The node-centred baselines reproduce the overall

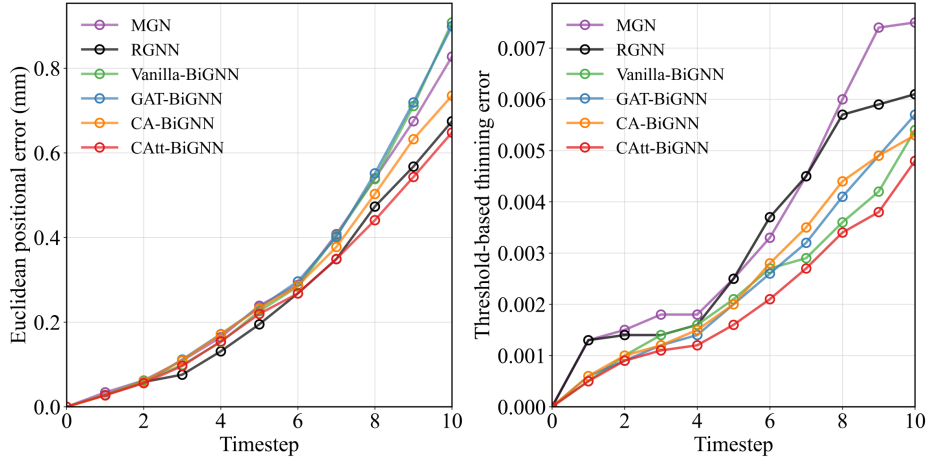


Figure 9: Dome case: evolution of test-set mean errors over the 10 autoregressive rollout transitions. (a) Euclidean positional error in mm. (b) Thresholded thinning error computed over elements whose FE reference thinning magnitude exceeds the selected threshold.

shape but show visible error concentrations in regions with high curvature and geometric transition. Vanilla-BiGNN improves the thinning field in these regions, which is consistent with the quantitative improvement in element-level metrics. However, its displacement prediction remains less accurate. This suggests that the bipartite graph formulation reduces interpolation errors between nodes and elements. Nevertheless, the coupling between nodal and elemental states is not effectively learnt. Consequently, errors originating in one field tend to propagate to the other through the message-passing process. This behaviour is evident in the figure, where the high-error regions in the thinning and displacement fields for Vanilla-BiGNN exhibit similar spatial locations and patterns. The attention-based variants reduce some of these errors by assigning nonuniform weights to node–element interactions. Among them, CAtt-BiGNN gives the most balanced visual agreement with the FE reference across both displacement and thinning fields.

The prediction results for additional dome test cases are presented in Appendix Appendix A, and the corresponding temporal rollout predictions are shown in Appendix Appendix B.

8.2. Corner-shaped case study

The corner-shaped case study involves larger graphs and sharper geometric transitions than the dome-shaped case. All models in this comparison

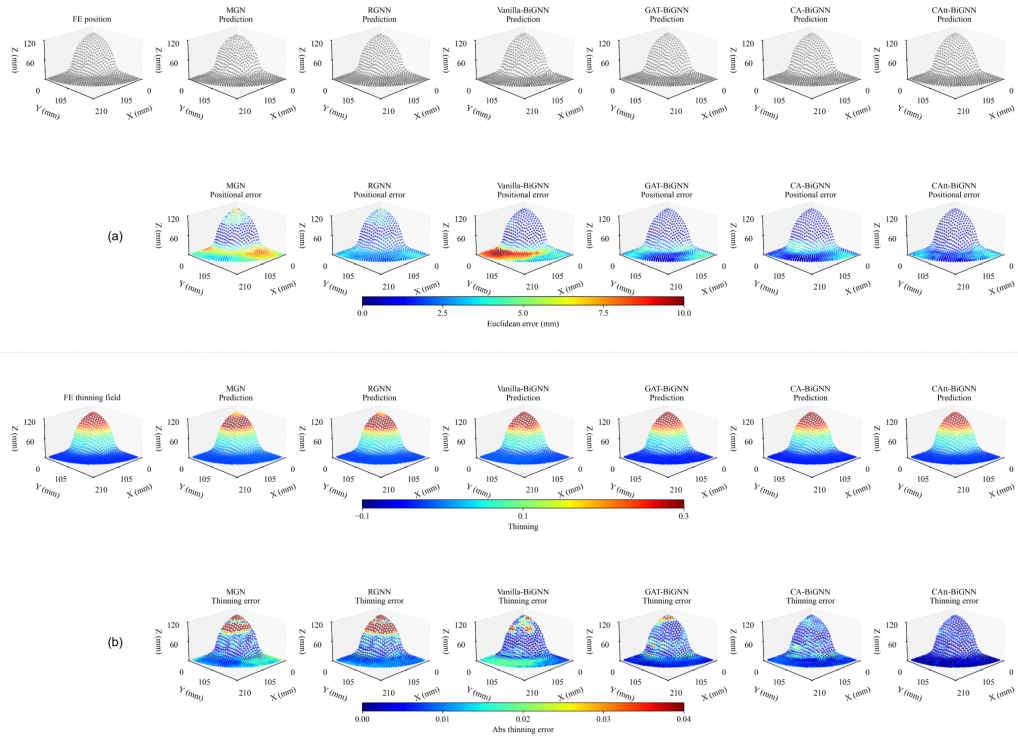


Figure 10: Final-timestep visual comparison for a representative dome test case. Columns show the FE reference and predictions from MGN, RGNN, Vanilla-BiGNN, GAT-BiGNN, CA-BiGNN, and CAtt-BiGNN. Panel (a) compares deformed nodal positions and Euclidean position-error maps. Panel (b) compares elemental thinning fields and absolute thinning-error maps. Colour bars indicate position error in mm and dimensionless thinning error.

therefore use a downsampling and upsampling mechanism, so the ablation focuses on how the bipartite representation and attention mechanism behave within a hierarchical graph architecture.

Baseline models. Six model configurations are evaluated: (a) UMGN, which extends MeshGraphNet by incorporating a downsampling and upsampling mechanism. (b) RUGNN, which is UMGN equipped with recurrent updates to better capture temporal dependencies [21]. (c) Vanilla-BiUGNN, our BiGNN variant that incorporates bipartite graph construction together with a hierarchical downsampling and upsampling mechanism, but without any attention-based aggregation functions. (d) GAT-BiUGNN, which extends Vanilla-BiUGNN with GAT-based attention aggregation. (e) CA-BiUGNN, which extends Vanilla-BiUGNN with cross-attention-based aggregation. (f) The proposed CAtt-BiUGNN model, which extends Vanilla-BiUGNN with the designed edge-based cross-attention aggregation, following the method introduced in Section 7. Specifically, the main difference between CA-BiUGNN and our proposed CAtt-BiUGNN is that CA-BiUGNN computes the Key matrix from source node or element features, whereas CAtt-BiUGNN derives them from edge features.

Among these comparative models, UMGN and RUGNN are treated as external baselines, while Vanilla-BiUGNN, GAT-BiUGNN, and CA-BiUGNN represent the ablation variants. All models use the recommended hyperparameters and the same GPU setup described in Section 6. Table 3 summarises the results.

Evaluation metrics. Each simulation consists of ten rollout timesteps. Similar to the dome-shaped case study, dual outputs are produced, namely displacement fields at the nodal level and thinning fields at the element level. The evaluation metrics follow those used for the dome-shaped case study in Section 8.1.

Results. Table 3 reports the final-timestep results for the corner-shaped case study. All relative changes are computed with respect to UMGN. Compared with UMGN, Vanilla-BiUGNN substantially improves the thinning metrics and also reduces the displacement errors. This again supports the value of representing thinning directly on element vertices. However, Vanilla-BiUGNN remains less accurate than RUGNN on the displacement metrics, showing that the hierarchical bipartite representation still requires an effective coupling mechanism to update nodal states robustly.

Table 3: Ablation study for the corner case study at the final rollout timestep.

Metric	UMGN	RUGNN	Vanilla-BiUGNN	GAT-BiUGNN	CA-BiUGNN	CAtt-BiUGNN (proposed)
Displacement evaluation metrics						
Mean positional	3.1507	2.0414	2.1734	2.3318	2.2001	1.8320
Euclidean error (mm)		(-35.2%)	(-31.0%)	(-26.0%)	(-30.2%)	(-41.8%)
Position MAE (mm)	1.2906	0.8982	0.9147	0.9471	0.9019	0.7560
		(-30.4%)	(-29.1%)	(-27.0%)	(-30.1%)	(-41.4%)
Thinning evaluation metrics						
Threshold-based thinning error	0.0052	0.0054	0.0033	0.0030	0.0029	0.0027
		(+3.8%)	(-36.5%)	(-42.3%)	(-44.2%)	(-48.1%)
Top 1% thinning COM	27.1670	18.7023	7.0291	6.1168	4.9398	5.3413
		(-31.2%)	(-74.1%)	(-77.5%)	(-81.8%)	(-80.3%)
Top 1% relative thinning error	27.6%	13.17%	7.83%	6.16%	8.19%	5.51%
		(-52.2%)	(-71.6%)	(-77.7%)	(-70.3%)	(-80.0%)

* Values in parentheses denote the relative change (%) with respect to the UMGN baseline (lower is better).

CAtt-BiUGNN achieves the best performance in four of the five reported metrics, reducing the mean positional Euclidean error by 41.8%, position MAE by 41.4%, thresholded thinning error by 48.1%, and top-1% relative thinning error by 80.0% relative to UMGN. CA-BiUGNN gives the lowest top-1% COM distance, indicating that conventional cross-attention can localise the most thinned region effectively in this metric. However, CAtt-BiUGNN provides the strongest overall accuracy across displacement and thinning measures.

These results support the edge-aware attention design in the hierarchical setting. In the corner case, deformation depends strongly on local geometric relations around the corner radius and contact regions. By deriving attention information from directed edge features, CAtt-BiUGNN can modulate node-element messages using these local geometric cues. This helps the model combine element-level thinning prediction with accurate nodal displacement prediction over a larger graph.

Next, we examine the effect of the different attention mechanisms used

in the ablation variants. GAT-BiUGNN does not show meaningful improvements over Vanilla-BiUGNN in either displacement or thinning prediction. This indicates that GAT-style self-attention is not effective for modelling the asymmetric and directional interactions between nodes and elements in a bipartite graph structure. CA-BiUGNN, which replaces GAT with a cross-attention formulation, exhibits a different behaviour. It improves the prediction of thinning localisation but does not improve displacement accuracy. This suggests that although cross-attention is beneficial for weighting element–node messages when predicting elemental fields, it does not fully capture the coupling required to update nodal displacements. One possible explanation is that CA-BiUGNN computes the Key and Value matrices from source node features. This limits the attention mechanism’s ability to encode geometric and deformation cues that are inherently edge-related. As a result, the learned attention weights only partially reflect the physical interactions that govern the deformation process.

In contrast, our proposed CAtt-BiUGNN achieves consistent improvements over the BiUGNN variants in both displacement and thinning metrics. By computing the Key and Value matrices from edge features, CAtt-BiUGNN incorporates richer geometric and deformation context into the attention process. This allows the model to assign more physically meaningful weights during message aggregation, leading to a more accurate representation of node–element coupling.

Figure 11 presents the evolution of Euclidean positional error and threshold-based thinning error over all 10 rollout timesteps for the corner-shaped case study. CAtt-BiUGNN consistently outperforms both the baseline models (UMGN and RUGNN) and the Vanilla-BiUGNN variant, confirming the benefit of incorporating cross-attention within the hierarchical bipartite graph architecture.

Figure 12 shows the final rollout predictions for the corner-shaped case. The hierarchical node-centred baselines capture the global shape but show larger errors around the corner radius and high-curvature regions. Vanilla-BiUGNN reduces the thinning error by representing thinning on element vertices, but some displacement error remains. The attention-based variants improve the spatial distribution of the predictions by weighting node–element interactions nonuniformly. CAtt-BiUGNN provides the most balanced prediction across displacement and thinning fields, particularly around the corner and contact-driven deformation regions. The visual comparison therefore supports the same conclusion as Table 3: the hierarchy improves propaga-

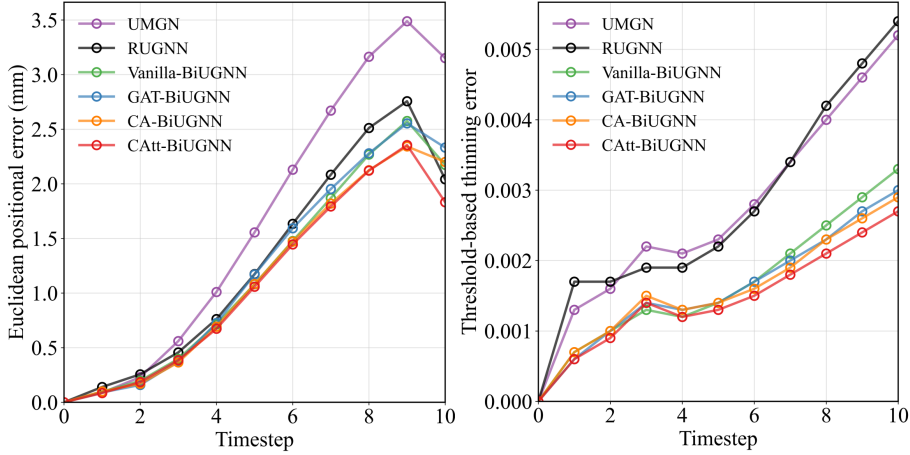


Figure 11: Corner case: evolution of test-set mean errors over the 10 autoregressive rollout transitions. (a) Euclidean positional error in mm. (b) Thresholded thinning error computed over elements whose FE reference thinning magnitude exceeds the selected threshold.

tion over the larger mesh, while edge-aware cross-attention improves the local coupling within that hierarchy.

Figure 13 shows the node-to-element attention weights computed at the final processor layer of the trained CAtt-BiUGNN model. The results are compared against those from the GAT-BiUGNN and CA-BiUGNN models.

Figure 13 visualises the deviation of the learned node-to-element attention weights from uniform mean aggregation. For an element vertex i , the uniform attention weight is $1/|\mathcal{N}(i)|$, where $\mathcal{N}(i)$ denotes the set of mesh nodes connected to element i . The plotted quantity is therefore

$$\Delta\alpha_{v \rightarrow i, L}^{N_p} = \alpha_{v \rightarrow i, L}^{N_p} - \frac{1}{|\mathcal{N}(i)|}. \quad (58)$$

Positive values indicate node-to-element edges receiving greater weight than uniform aggregation, whereas negative values indicate suppressed edges.

The GAT-BiUGNN maps show relatively weak case-to-case variation, which is consistent with the limited improvement of GAT-style aggregation in Table 3. CA-BiUGNN introduces more variation and gives strong thinning-localisation performance, as reflected by its low top-1% COM distance. CAtt-BiUGNN produces more spatially structured attention patterns near geometric transitions and thinning-prone regions. These maps can be interpreted as qualitative evidence that edge-aware attention adapts to local

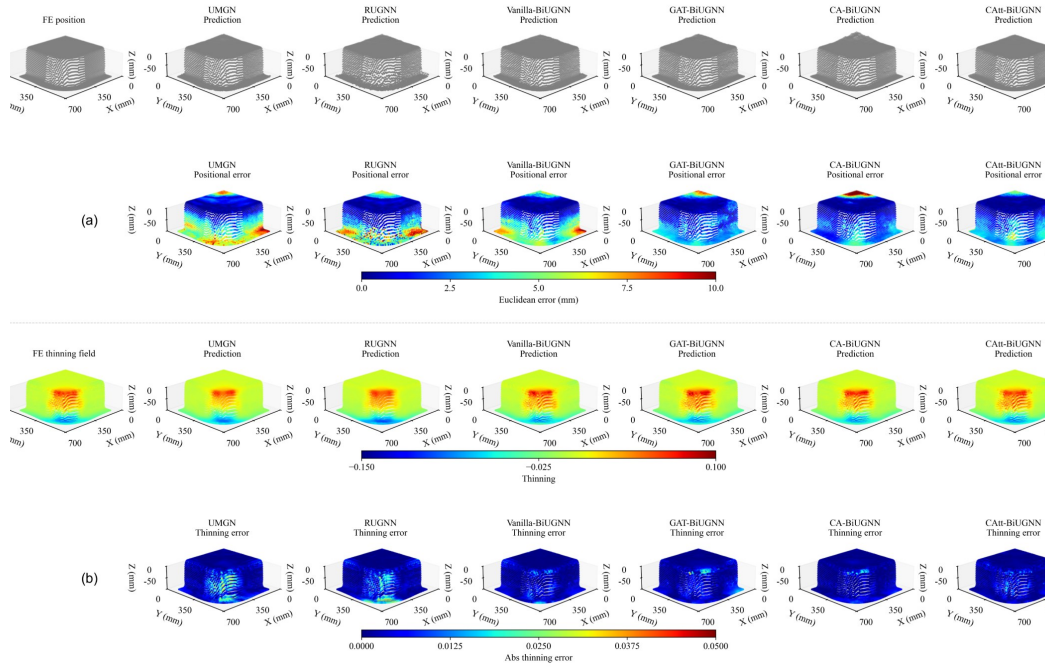


Figure 12: Final-timestep visual comparison for a representative corner test case. Columns show the FE reference and predictions from UMGNN, RUGNN, Vanilla-BiUGNN, GAT-BiUGNN, CA-BiUGNN, and CAtt-BiUGNN. Panel (a) compares deformed nodal positions and Euclidean position-error maps. Panel (b) compares elemental thinning fields and absolute thinning-error maps. Colour bars indicate position error in mm and dimensionless thinning error.

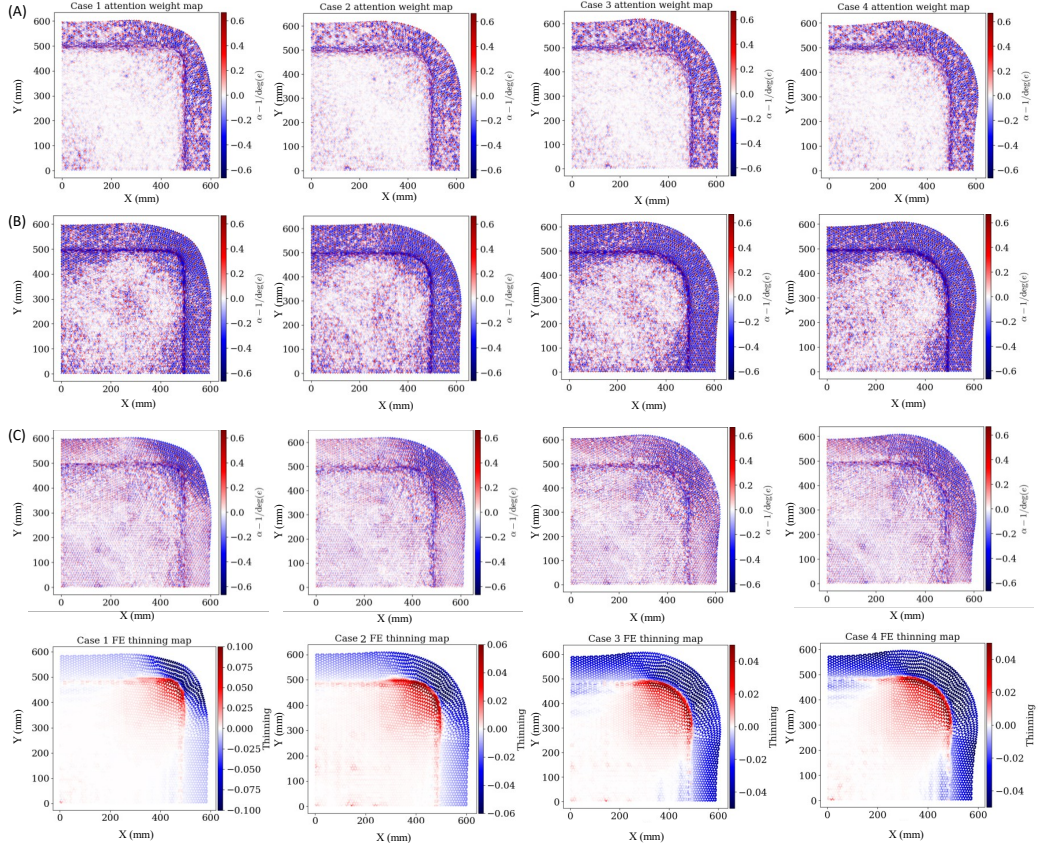


Figure 13: Attention-deviation maps at the last processor layer and final rollout timestep for four corner test cases. Rows (A)–(C) show $\alpha_{v \rightarrow i, L}^{N_p} - 1/|\mathcal{N}(i)|$ for GAT-BiUGNN, CA-BiUGNN, and CAtt-BiUGNN, respectively, where $\alpha_{v \rightarrow i, L}^{N_p}$ is the node-to-element attention weight and $\mathcal{N}(i)$ is the set of mesh nodes connected to element i . The bottom row shows the corresponding FE thinning fields for qualitative comparison.

node–element geometry. They should not be described as proof of enforced physical consistency. They help explain why edge-aware message weighting improves the overall predictive balance between nodal displacement and elemental thinning.

The prediction results on different test sets for the corner case study are illustrated in Appendix C, and the temporal rollout prediction results are shown in Appendix D. Both appendices demonstrate that the predictions of the CAtt-BiUGNN model are closely aligned with the FE simulation results.

8.3. Comparison of different noise strategies

The noise-ablation study is separated from the baseline architecture comparison for two related reasons. First, in this implementation, the perturbation is introduced only through the nodal displacement-increment input. Its effect is therefore expected to be most direct on displacement rollout, whereas its influence on elemental thinning prediction is indirect, because thinning is predicted on element vertices and is affected through the learned node–element coupling during rollout. Second, the appropriate noise perturbation form and scale may depend on the model architecture. Applying independently tuned noise settings to different baselines would make it difficult to distinguish architectural effects from noise-strategy tuning. Therefore, the baseline comparison is performed under a common noise-free training setting, while noise injection is analysed separately as an optional rollout-stabilisation strategy for the proposed CAtt-BiUGNN architecture, with the noise configuration selected using the validation set.

Based on this separation, the noise-ablation experiment is conducted on the corner-shaped case study using CAtt-BiUGNN as the reference architecture. The architecture, training dataset, and evaluation protocol are kept unchanged, and only the training perturbation strategy is varied. Three settings are compared: no noise, uniform Gaussian noise, and the adaptive Gaussian noise strategy described in Section 7.2. For each noise setting, the noise scale is selected using validation experiments only; the test set is not used for selecting noise parameters. The results are reported in Table 4.

Table 4 evaluates noise injection as a rollout-stabilisation strategy for the corner-shaped case. The results show that the effect of noise injection is metric-dependent in the present case. Since the perturbation is introduced through the nodal displacement-increment input, the largest error reduction is observed in the displacement-based metrics. Its influence on elemental

Table 4: Noise ablation study for the corner case at the final rollout timestep.

Metric	No noise	Uniform Gaussian noise	Adaptive Gaussian noise
Displacement evaluation metrics			
Mean positional Euclidean error (mm)	1.8320	0.4795 (-73.83%)	0.4708 (-74.30%)
Position MAE (mm)	0.7560	0.2220 (-70.63%)	0.2137 (-71.73%)
Thinning evaluation metrics			
Threshold-based thinning error	0.0027	0.0023 (-14.81%)	0.0020 (-25.93%)
Top 1% COM thinning (mm)	5.3413	6.0866 (+13.95%)	5.2024 (-2.60%)
Top 1% relative thinning error	5.51%	5.07% (-7.99%)	3.85% (-30.13%)

* Values in parentheses denote the relative change (%) with respect to the no-noise baseline (lower is better).

thinning metrics is less direct, because thinning is predicted on element vertices and is mediated by the learned node–element coupling during rollout. Uniform Gaussian noise reduces the displacement errors but increases the top-1% COM thinning distance, suggesting that a spatially uniform perturbation may adversely affect the localisation of critical thinning regions. By contrast, the adaptive strategy gives a more balanced improvement across displacement and thinning-related metrics, although the improvement in thinning localisation remains smaller than that in displacement prediction.

This behaviour is consistent with the motivation in Section 7.2. Uniform noise applies the same perturbation scale to all nodes, regardless of local deformation magnitude. In contrast, the adaptive strategy applies stronger perturbations to nodes with smaller displacement increments and weaker perturbations to nodes with larger displacement increments. This is useful in sheet forming because slowly moving or near-contact regions can still strongly influence subsequent contact descriptors and deformation evolution. The adaptive perturbation therefore improves rollout robustness without excessively disturbing regions that already contain clear deformation signals.

9. Conclusion

This study was motivated by the observation that node-centred formulations commonly used in mesh-based graph surrogates do not explicitly represent the node–element information flow in finite element simulations of sheet material forming. The finite element update couples nodal kinematics with element-level deformation measures, whereas node-centred graph surrogates place the primary learned states on mesh nodes. This makes the representation less direct for element-level targets such as thinning, strain, or stress. In

such settings, elemental quantities are often recovered through interpolation or post-processing, which can introduce additional errors and may obscure the node–element coupling structure that underlies the finite element update.

This work proposed CAtt-BiGNN, a cross-attention-based bipartite graph neural network for coupled prediction of nodal and elemental fields in sheet material forming. The proposed graph represents mesh nodes and elements as distinct graph entities. Nodal displacement increments are decoded from node states, while elemental thinning values are decoded from element states. Directed node–element edges provide the communication pathway through which the model learns interactions between nodal kinematic states and elemental deformation states. This representation is finite-element-inspired, but the model remains a learned surrogate rather than an explicitly constrained finite element solver.

The proposed edge-aware cross-attention processor improves node–element message passing by conditioning adaptive coupling weights on directed geometric edge features. This allows the model to modulate interactions according to local geometric relations between nodes and elements. For larger forming graphs, CAtt-BiUGNN extends the same bipartite processor with downsampling, upsampling, and skip connections to improve information propagation.

The numerical results support the proposed design. In the smaller-graph forming case, CAtt-BiGNN improves the overall balance between nodal displacement and elemental thinning prediction relative to both node-centred mesh baselines and bipartite ablation variants. In the larger-graph forming case, CAtt-BiUGNN provides substantial error reductions relative to the hierarchical mesh baseline UMGNN and achieves the strongest overall performance among the hierarchical bipartite variants. The adaptive-noise ablation further shows that spatially scaled perturbations can improve autoregressive rollout robustness for the hierarchical model.

Overall, the results support three conclusions. First, representing nodal and elemental quantities on separate graph entities provides a more natural discretisation for coupled displacement–thinning prediction than node-centred graph formulations. Second, edge-aware cross-attention is more effective than generic attention mechanisms for modelling directional node–element interactions, because the attention weights are conditioned on local geometric relations. Third, hierarchical propagation improves the scalability of the bipartite formulation on larger forming meshes. These findings suggest that FE-inspired graph representations provide a promising direction for

surrogate modelling of large-deformation sheet material forming, particularly when both nodal kinematics and elemental manufacturability indicators are required.

The present study establishes CAtt-BiGNN and CAtt-BiUGNN as FE-inspired surrogate frameworks for geometry-driven sheet-forming prediction. The evaluation focuses on tool-geometry variations across the sampled design space, which is central to manufacturability assessment and tool-design studies in sheet material forming. Future work will broaden the dataset construction and graph input space to include material descriptors, forming-process parameters, more diverse forming geometries, and mesh-topology variations. Integrating the surrogate into optimisation workflows may further support rapid manufacturability assessment and design-space exploration.

Acknowledgement

The authors acknowledge funding support from UKRI (UKRI221: AI-Driven Design for Forming High-Performance Vehicle Parts), as well as PhD scholarships from Imperial College London. The authors would like to thank ESI Group for their technical support with the PAM-STAMP software. For the purpose of open access, the author has applied a Creative Commons Attribution (CC BY) license to any Author Accepted Manuscript version arising.

Appendix A. Prediction results on dome-shaped case study

Figure A.14 presents the prediction performance of the CAtt-BiGNN model trained with adaptive Gaussian noise. Three representative dome-shaped cases, corresponding to the smallest, median, and largest dome radii within the design space, are displayed. Across all three cases, the predicted geometries are in close agreement with the FE simulation results, with Euclidean positional errors at the final timestep remaining below approximately 5 mm. The predicted thinning fields also exhibit a high level of consistency with the FE ground truth, capturing the spatial variation of the thinning field with strong fidelity. These results suggest that the model maintains reliable predictive accuracy across dome geometries with substantially different curvature conditions.

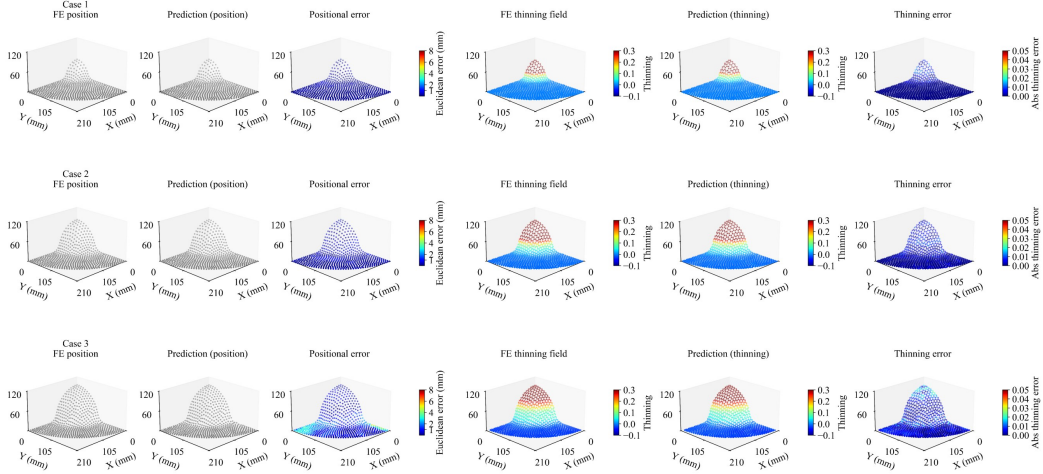


Figure A.14: Final-timestep predictions of CAtt-BiGNN trained with adaptive Gaussian noise for three dome test cases. Each row corresponds to one design case. Columns show FE reference position, predicted position, Euclidean position error, FE thinning field, predicted thinning field, and absolute thinning error.

Appendix B. Temporal rollout prediction results on dome-shaped case study

Figure B.15 illustrates the temporal rollout performance of the CAtt-BiGNN model trained with adaptive Gaussian noise. Two dome-shaped cases, corresponding to the smallest and largest dome radii, are displayed. The results show that the model produces temporally coherent and stable predictions throughout the rollout sequence. The deformation and thinning fields evolve smoothly over time and remain closely aligned with the FE simulation results across all timesteps. The differences between the predicted and ground-truth thinning fields are minor, indicating that the model can effectively maintain its predictive accuracy during autoregressive rollout without noticeable error accumulation.

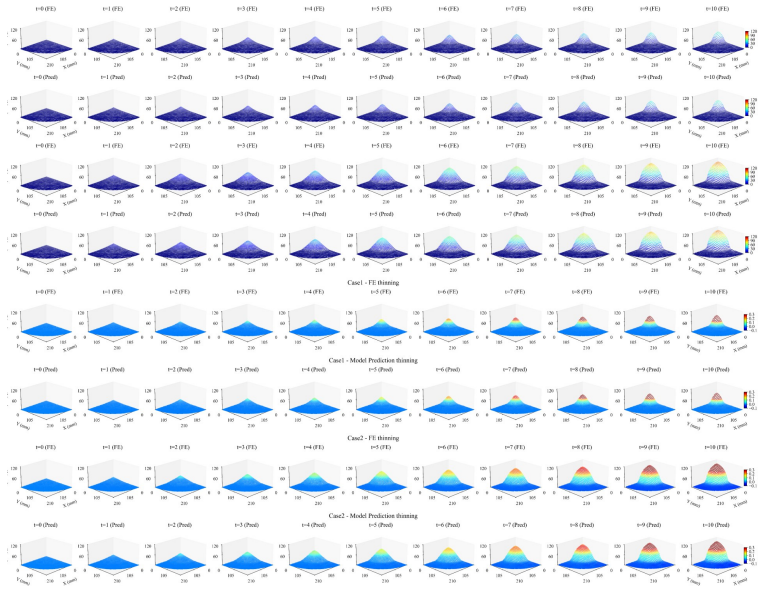


Figure B.15: Temporal rollout predictions of CAtt-BiGNN trained with adaptive Gaussian noise for two dome test cases. Columns correspond to rollout timesteps. Rows compare FE and predicted deformed positions for each case, followed by FE and predicted thinning fields. The figure illustrates temporal consistency during autoregressive rollout.

Appendix C. Prediction results on corner-shaped case study

Figure C.16 presents the prediction performance of the CAtt-BiUGNN model trained with adaptive Gaussian noise. Three representative cases situated at the boundaries of the design space are displayed. These cases were selected to assess the model’s performance under the smallest and largest combinations of height and planar radius.

Across all cases, the predicted geometries closely match the FE-simulated shapes, with Euclidean positional errors remaining below approximately 2.5 mm. The predicted thinning fields are also highly consistent with the FE ground truth, and the corresponding error maps show absolute error values mostly below 0.03. These results confirm that the model maintains strong predictive accuracy across a wide range of geometric variations.

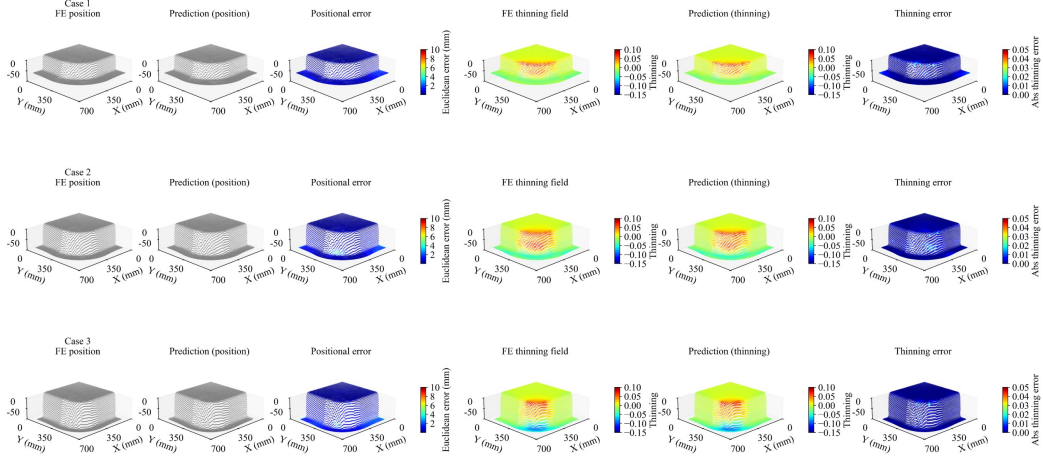


Figure C.16: Final-timestep predictions of CAtt-BiUGNN trained with adaptive Gaussian noise for three corner test cases. Each row corresponds to one design case. Columns show FE reference position, predicted position, Euclidean position error, FE thinning field, predicted thinning field, and absolute thinning error.

Appendix D. Temporal rollout prediction results on corner-shaped case study

Figure D.17 illustrates the temporal rollout performance of the CAtt-BiUGNN model trained with adaptive Gaussian noise. Two representative test cases, consistent with those in Appendix C, are selected to assess the stability and accuracy of the model’s autoregressive predictions. The visualisations show the evolution of the predicted deformation and thinning fields from the initial to the final timestep.

The predicted sequences exhibit smooth and realistic temporal transitions that align closely with the FE results. The differences between the predicted and ground-truth thinning fields remain negligible throughout the rollout, demonstrating that the model preserves high accuracy across all timesteps without error accumulation.

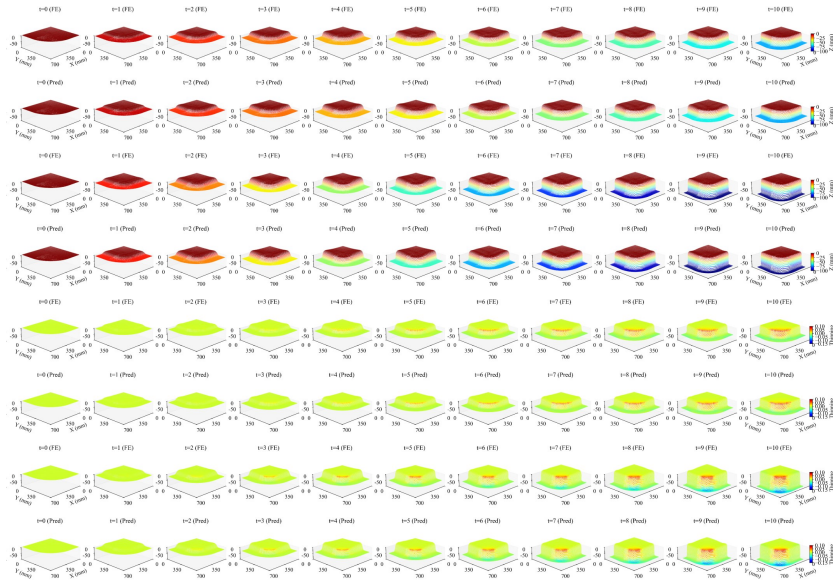


Figure D.17: Temporal rollout predictions of CAtt-BiUGNN trained with adaptive Gaussian noise for two corner test cases. Columns correspond to rollout timesteps. Rows compare FE and predicted deformed positions for each case, followed by FE and predicted thinning fields. The figure illustrates the stability of autoregressive predictions across the forming process.

References

- [1] D. Politis, A. Foster, N. Li, L. Wang, J. Lin, A. Foster, D. Szegda, Prediction of thinning behavior for complex-shaped, lightweight alloy panels formed through a hot stamping process, in: *Advanced High Strength Steel and Press Hardening: Proceedings of the 2nd International Conference (ICHSU2015)*, World Scientific, 2016, pp. 395–401.
- [2] T. J. R. Hughes, *The Finite Element Method: Linear Static and Dynamic Finite Element Analysis*, Prentice-Hall, Englewood Cliffs, NJ, 1987.
- [3] K. Bathe, *Finite Element Procedures*, Prentice Hall, 2006.
URL <https://books.google.co.uk/books?id=rWvfgICf08C>
- [4] H. R. Attar, A. Foster, N. Li, Development of a deep learning platform for sheet stamping geometry optimisation under manufacturing con-

- straints, *Engineering Applications of Artificial Intelligence* 123 (2023) 106295.
- [5] H. Zhou, H. Li, Y. Zhao, P. R. Childs, N. Li, Image-based artificial intelligence-driven modelling for blank shape optimisation in sheet metal forming, *Materials & Design* (2025) 114302.
- [6] G. E. Karniadakis, I. G. Kevrekidis, L. Lu, P. Perdikaris, S. Wang, L. Yang, Physics-informed machine learning, *Nature Reviews Physics* 3 (2021) 422–440. doi:10.1038/s42254-021-00314-5.
- [7] Y. Zhao, H. Li, H. Zhou, H. R. Attar, T. Pfaff, N. Li, A review of graph neural network applications in mechanics-related domains, *Artificial Intelligence Review* 57 (11) (2024) 315.
- [8] J. Willard, X. Jia, S. Xu, M. Steinbach, V. Kumar, Integrating physics-based modeling with machine learning: A survey (03 2020). doi:10.48550/arXiv.2003.04919.
- [9] V. K. Dubey, C. E. Haese, O. Gültekin, D. Dalton, M. K. Rausch, J. Fuhs, Graph neural network surrogates for contacting deformable bodies with necessary and sufficient contact detection, *Computer Methods in Applied Mechanics and Engineering* 448 (2026) 118413. doi:https://doi.org/10.1016/j.cma.2025.118413.
- [10] L. Xing, P. Gardoni, G. Song, Y. Zhou, Deep learning-based surrogate capacity models and multi-objective fragility estimates for reinforced concrete frames, *Computer Methods in Applied Mechanics and Engineering* 440 (2025) 117928. doi:https://doi.org/10.1016/j.cma.2025.117928.
- [11] A. Sanchez-Gonzalez, J. Godwin, T. Pfaff, R. Ying, J. Leskovec, P. Battaglia, Learning to simulate complex physics with graph networks, in: *International conference on machine learning*, PMLR, 2020, pp. 8459–8468.
- [12] T. Pfaff, A. Sanchez-Gonzalez, P. W. Battaglia, et al., Learning mesh-based simulation with graph neural networks, *International Conference on Learning Representations* (2021).

- [13] Z. Wu, S. Pan, F. Chen, G. Long, C. Zhang, P. S. Yu, A comprehensive survey on graph neural networks, *IEEE transactions on neural networks and learning systems* 32 (1) (2020) 4–24.
- [14] M. M. Bronstein, J. Bruna, T. Cohen, P. Veličković, Geometric deep learning: Grids, groups, graphs, geodesics, and gauges, *arXiv preprint arXiv:2104.13478* (2021).
- [15] P. Veličković, Everything is connected: Graph neural networks, *Current Opinion in Structural Biology* 79 (2023) 102538.
- [16] J. Zhou, G. Cui, S. Hu, Z. Zhang, C. Yang, Z. Liu, L. Wang, C. Li, M. Sun, Graph neural networks: A review of methods and applications, *AI open* 1 (2020) 57–81.
- [17] J. Gilmer, S. S. Schoenholz, P. F. Riley, O. Vinyals, G. E. Dahl, Neural message passing for quantum chemistry, in: *International conference on machine learning*, Pmlr, 2017, pp. 1263–1272.
- [18] D. Dalton, D. Husmeier, H. Gao, Physics-informed graph neural network emulation of soft-tissue mechanics, *Computer Methods in Applied Mechanics and Engineering* 417 (2023) 116351.
- [19] Y. Fei, S. Qin, W. Liao, H. Guan, X. Lu, Graph neural network-assisted evolutionary algorithm for rapid optimization design of shear-wall structures, *Advanced Engineering Informatics* 65 (2025) 103129.
- [20] L. Patrignani, S. T. Pinho, Graph neural networks with hybrid local-global attention for effective prediction of mechanical response in structures, *Computer Methods in Applied Mechanics and Engineering* 452 (2026) 118753. doi:<https://doi.org/10.1016/j.cma.2026.118753>.
- [21] Y. Zhao, Q. Chen, H. Li, H. Zhou, H. R. Attar, T. Pfaff, T. Wu, N. Li, Recurrent u-net-based graph neural network (rugnn) for accurate deformation predictions in sheet material forming, *Advanced Engineering Informatics* 69 (2026) 104021.
- [22] Y. Zhao, H. Li, H. Zhou, H. R. Attar, T. Pfaff, N. Li, Rapid prediction of material deformation in hot stamping of battery box geometries using graph neural network, in: *Journal of Physics: Conference Series*, Vol. 3104, IOP Publishing, 2025, p. 012057.

- [23] Q. Chen, J. Cao, W. Lin, S. Zhu, S. Wang, Predicting dynamic responses of continuous deformable bodies: A graph-based learning approach, *Computer Methods in Applied Mechanics and Engineering* 420 (2024) 116669.
- [24] N. Black, A. R. Najafi, Learning finite element convergence with the multi-fidelity graph neural network, *Computer Methods in Applied Mechanics and Engineering* 397 (2022) 115120.
- [25] P. Battaglia, R. Pascanu, M. Lai, D. Jimenez Rezende, et al., Interaction networks for learning about objects, relations and physics, *Advances in neural information processing systems* 29 (2016).
- [26] A. Sanchez-Gonzalez, N. Heess, J. T. Springenberg, J. Merel, M. Riedmiller, R. Hadsell, P. Battaglia, Graph networks as learnable physics engines for inference and control, in: *International conference on machine learning*, PMLR, 2018, pp. 4470–4479.
- [27] X. Fu, F. Zhou, D. Peddireddy, Z. Kang, M. B.-G. Jun, V. Aggarwal, An finite element analysis surrogate model with boundary oriented graph embedding approach for rapid design, *Journal of Computational Design and Engineering* 10 (3) (2023) 1026–1046.
- [28] H. Zhou, Y. Zhao, H. Li, T. Pfaff, N. Li, A multi-level graph-based surrogate model for real-time high-fidelity sheet forming simulations, *Advanced Engineering Informatics* 66 (2025) 103458.
- [29] S. Deshpande, S. Bordas, J. Lengiewicz, Magnet: A graph u-net architecture for mesh-based simulations, *arXiv preprint arXiv:2211.00713* (2022).
- [30] T. Li, S. Zou, X. Chang, L. Zhang, X. Deng, Finite volume graph network (fvgn): Predicting unsteady incompressible fluid dynamics with finite volume informed neural network, *arXiv preprint arXiv:2309.10050* (2023).
- [31] R. Gao, I. K. Deo, R. K. Jaiman, A finite element-inspired hypergraph neural network: Application to fluid dynamics simulations, *Journal of Computational Physics* 504 (2024) 112866. doi:<https://doi.org/10.1016/j.jcp.2024.112866>.

- [32] T. Belytschko, W. K. Liu, B. Moran, K. Elkhodary, *Nonlinear finite elements for continua and structures*, John Wiley & sons, 2014.
- [33] A. Vaswani, N. Shazeer, N. Parmar, J. Uszkoreit, L. Jones, A. N. Gomez, Ł. Kaiser, I. Polosukhin, Attention is all you need, *Advances in neural information processing systems* 30 (2017).
- [34] P. Veličković, G. Cucurull, A. Casanova, A. Romero, P. Lio, Y. Bengio, Graph attention networks, *arXiv preprint arXiv:1710.10903* (2017).
- [35] K. Zheng, D. J. Politis, L. Wang, J. Lin, A review on forming techniques for manufacturing lightweight complex—shaped aluminium panel components, *International Journal of Lightweight Materials and Manufacture* 1 (2) (2018) 55–80.
- [36] K. Zheng, J. Lee, D. J. Politis, N. Li, J. Lin, T. A. Dean, An analytical investigation on the wrinkling of aluminium alloys during stamping using macro-scale structural tooling surfaces, *The International Journal of Advanced Manufacturing Technology* 92 (1) (2017) 481–495.
- [37] N. Li, C. Sun, N. Guo, M. Momhamed, J. Lin, M. Takeki, Damage investigation of boron steel at hot stamping conditions, *Procedia Engineering* 81 (2014) 1744–1749.
- [38] Dassault Systèmes, United States of America, *Getting Started with Abaqus Interactive Edition* (2008).
- [39] J. L. D. Z. Marciniak, S. J. Hu, *Mechanics of Sheet Metal Forming*, Butterworth-Heinemann, Great Britain, 2002.
- [40] W. Hosford, R. Caddell, *Metal Forming Mechanics and Metallurgy*, 2011. doi:10.1017/CBO9780511811111.
- [41] B. Liang, S. Gao, W. Zhang, An integrated preforming-performance model for high-fidelity performance analysis of cured woven composite part with non-orthogonal yarn angles, *Chinese Journal of Aeronautics* 35 (6) (2022) 367–378.
- [42] H. R. Attar, H. Zhou, A. Foster, N. Li, Rapid feasibility assessment of components to be formed through hot stamping: A deep learning approach, *Journal of Manufacturing Processes* 68 (2021) 1650–1671. doi:<https://doi.org/10.1016/j.jmapro.2021.06.011>.

- [43] M. Mohamed, N. Li, L. Wang, O. E. Fakir, J. Lin, T. Dean, J. Dear, An investigation of a new 2d cdm model in predicting failure in hfqing of an automotive panel, in: 4th International Conference on New Forming Technology (ICNFT 2015), EDP Sciences, 2015, p. 05011.